MOLECULAR DYNAMICS SIMULATION STUDY OF CARBON DIOXIDE - HYDROCARBON MIXTURES UNDER CONFINEMENT

A Thesis

by

MUHAMMAD HAMZA

Submitted to the Office of Graduate and Professional Studies of
Texas A&M University
in partial fulfillment of the requirements for the degree of

MASTER OF SCIENCE

Chair of Committee,	Ioannis Economou
Committee Members,	Ahmed Abdala
	Ahmed Abdel-Wahab
	Eyad Masad
Head of Department,	M. Nazmul Karim

August 2019

Major Subject: Chemical Engineering

ABSTRACT

Reducing carbon dioxide emissions in an attempt to control global warming is a critical issue being addressed at global level today. One method of regulating the amount of CO_2 in the atmosphere is by re-injecting CO_2 into reservoirs, thus in turn also improving the overall recovery of oil and gas. This is an enhanced oil/gas recovery technique which has received a lot of attention in industry. In this work, a study of the phenomena that allows for improved hydrocarbon recovery using CO_2 injection into reservoir pores is presented. Additionally, an attempt to understand the effect of mixture density, concentration, temperature, moisture and the pore material on such systems will be discussed. Furthermore, the ways in which diffusivity of fluid behaves at the center of the pore as well as towards the pore walls is explored in detail in this work.

All systems that have been simulated represent a canonical ensemble. Hence, at any given time, the number of molecules, the volume of the pore, and the temperature remain the same as specified at the beginning of a simulation. The work utilizes a methodology developed by Franco *et al.* to calculate the perpendicular self-diffusion co-efficient by obtaining the residence time from the integration of the survival probability. The methodology further allows for the calculation of the local self-diffusion coefficient in areas of interest as opposed to the global self-diffusion coefficient obtained from the commonly used Einstein relation.

Results indicate that all studied characteristics of a system have a significant effect on the mobility and the configuration of the fluid within pore. Furthermore, these characteristics have a greater pronounced effect of the diffusivity at the center of the pore and a lesser effect in the region towards the wall. Further calculating the parallel self-diffusion coefficient of the fluid in the same

systems analyzed in this work will provide even greater insight on the behavior of hydrocarbons within nanopores, in the presence of CO_2.

DEDICATION

I would like to dedicate this thesis to my mother who has been the backbone of my endeavors throughout my entire life.

ACKNOWLEDGEMENTS

I would like to acknowledge my entire committee. Thank you to my supervisor, Dr. *Ioannis Economou*, and to all my committee members, *Dr. Ahmed Abdala, Dr. Ahmed Abdel-Wahab* and *Dr. Eyad Masad* for allowing me to undertake this excellent research opportunity. I would also like to greatly thank, Dr. *Mirella Simoes Santos* for facilitating my entire research work by supporting me at every stage with her guidance and expertise. This work would not have been possible without her constant support. Furthermore, I would like to thank *Dr. Marcelo Castier* and *Dr. Luis Franco* for their guidance as well.

Thank you to my family and friends for all their support and encouragement. And finally, the biggest and foremost acknowledgment to Allah.

CONTRIBUTORS AND FUNDING SOURCES

Contributors

This work was supervised by a thesis committee consisting of Professor Ioannis Economou, Professor Ahmed Abdala, and Professor Ahmed Abdel-Wahab of the Chemical Engineering Program, and Professor Eyad Masad of the Mechanical Engineering Program of Texas A&M University at Qatar.

The code for perpendicular self-diffusion coefficient was co-developed with Dr. Mirella Santos of the Chemical Engineering Program and the code for application of SAFT-VR Mie in confinement was co-developed with Dr. Marcelo Castier and Dr. Luis Fernando Mercier Franco.

All other work conducted for the thesis was completed by the student independently.

Funding Sources

This work was also made possible by the National Priorities Research Program (NPRP) of Qatar National Research Fund (QNRF) under Grant Number NPRP8-1648-2-688. Its contents are solely the responsibility of the authors and do not necessarily represent the official views of the QNRF.

TABLE OF CONTENTS

Page

LIST OF FIGURES

Page

LIST OF TABLES

Page

CHAPTER I

INTRODUCTION

1.1 Background and Motivation

Today, global warming is a major issue being addressed at international level. CO_2 is one of the major constituents causing global warming. Thus, it is paramount to find a way to reduce carbon dioxide emissions into the environment by introducing carbon capture, utilization and storage (CCUS) processes. Techniques revolving around CCUS aim to reutilize CO_2 by recycling it into further meaningful products[1-3].

One such technique is known as CO_2 enhanced oil/gas recovery (EOR/EGR). This technique addresses two key matters: one, the storage of CO_2 and two, the recovery of oil and/or gas in the reservoir that the CO_2 is being deposited to. CO_2 is used as a working fluid in the tertiary recovery of the oil and/or gas. Studies show that the increment in recovery can be anywhere within the range of 8 – 16%, while sealing the CO_2 within the reservoir[4,5]. Such techniques have been extensively researched and developed for conventional reservoirs however, significant progress still needs to be made with respect to unconventional reservoirs where 40% of hydrocarbons remains trapped even after primary and secondary recovery[1,6-10].

Shale gas is a type of unconventional gas found in shale deposits. This shale gas can either be “free gas” trapped within the pores of the shale rock, or it can be adsorbed onto the surface of the pore[11]. Due to shale gas confinement in such tight pores, these fluids exhibit properties that would differ from the properties exhibited by the same fluids in bulk. As such, even after showcasing several different features of what is expected in bulk or even in conventional reservoirs, it is still extremely difficult to understand the complex behavior of such fluids under confinement. Understanding the properties of such fluids in these conditions can prove useful in

extracting relevant components from these reservoirs as well as obtaining a better prediction of reservoir production. Studies have shown that the desorption of the adsorbed gas can contribute to anywhere between 5 – 30% of the total gas production from shale reservoirs[12]. In this work, we worked on better understanding the behavior of relevant fluids under confinement by exploring the diffusivity and density changes that occur within systems of interest.

1.2 Objectives

In this work, we aimed to better understand the behavior of relevant fluids under confinement by exploring the diffusivity and density changes that occur within the systems of interest. The various objectives associated with the above aim are as follows:

1. Use molecular dynamics simulation to develop systems analogous to complex systems found in nature, subjected to underlying assumptions
2. Understand the general effect of confinement on relevant systems
3. Study the effect of various parameters on confined fluid properties of interest. These parameters include:
    1. Fluid density
    2. Fluid composition
    3. System temperature
    4. Type of substrate
    5. Pore size
    6. Moisture content within the system
4. Compare the results obtained from using molecular dynamics simulation with those obtained using an equation of state

CHAPTER II

LITERATURE REVIEW

2.1 Experimental Studies

Many experiments have been conducted to better understand the behavior of oil or gas components with CO_2 for EOR[13-17]. Experiments have shown that recovery of hydrocarbon is dependent on several factors such as the formation of the rock, pressure and temperature of reservoir, and the relative adsorption and desorption preference of CO_2 to alkanes[54]. This was proven through conducting gravimetric adsorption experiments to study the adsorption of methane, carbon dioxide and nitrogen on zeolite 13X at various pressures and temperatures. The isoteric heats of adsorption showed that carbon dioxide had the strongest adsorption and the substrate in question was a good candidate for CO_2 sequestration from flue gas.

Furthermore, it has been reported that adsorption and desorption of the fluid and the diffusion process play the most critical role in enhanced gas recovery and CO_2 sequestration[55]. Zhu *et al.* approximated the adsorption and desorption of CO_2 and N_2 across a coalbed, using an extended Langmuir isotherm. Mixtures of CO_2, CH_4 and N_2 were used to represent coalbed and injection gases. N_2 and CO_2 mixtures with high N_2 content resulted in faster initial CH_4 recovery, whereas mixtures with high CO_2 content resulted in slower initial CH_4 recovery. The trade-off found however was that greater time was required in separating the N_2 from the produced gas, whereas it took less time and effort to separate CO_2 from the produced gas.

Over the years, many experimental studies have been conducted to study the interaction of alkanes, CO_2, or their mixtures in different types of reservoir rocks. Duan *et al.*[56] studied the adsorption equilibrium of CO_2, CH_4 and their mixtures on the Sichuan basin shale from Nanchuan,

China. The substrate is characterized with high total organic carbon and inorganic minerals such as quartz and orthoclase, with wide pore size distribution ranges. The adsorption equilibrium isotherms were measured at different temperatures using the gravimetric method and the selectivity factor for CO_2 over CH_4 was estimated through the measured adsorption equilibrium data. The heat of adsorption, negative Gibbs free energy and the negative surface potential for CO_2 was found to be larger than that of CH_4, indicating that CO_2 adsorbs on to shale in a more highly ordered arrangement than CH_4. The adsorption capacity of CO_2 at all temperatures was found to be greater than the adsorption capacity of CH_4 in shale. At lower temperatures, the CO_2 formed multiple adsorption layers on the shale sample. The selectivity of the adsorption was found to be dependent on the pore material. High content of inorganic minerals favored the adsorption of CO_2, whereas high content of organic material favored the adsorption of CH_4.

Kang *et al.*[57] conducted an experimental study to measure the ability of organic-rich-shale samples to store carbon dioxide. An analytical method was used which interpreted pressure and volume in terms of porosity and Langmuir parameters of the shale sample. It was found that pore volume estimation is vital for CO_2 sequestration considerations. Furthermore, the majority of the up taken gas is stored via adsorption, depending on the pressure and temperature. Additionally, gas transport was found to be generally dominated by the adsorbed phase transport dynamics.

Gensterblum *et al.*[58] provided evidence on the competitive adsorption between H_2O, CO_2 and CH_4. The adsorption experiments were conducted on coal at different temperatures and pressures, under dry as well as moist conditions. It was deduced that functional groups containing oxygen atoms acted as the active sites and the competitive interactions for adsorption between CO_2, H_2O and CH_4 was due to volume displacement and not due to the type of gas. CO_2 was increasingly adsorbed, over CH_4 with increasing active sites as well as with increasing pressure,

while the preference of CO_2 adsorption decreased with increasing surface coverage. At low surface coverage, surface chemistry, pore size distribution and the pre-adsorbed water played a vital role with respect to the thermodynamic properties of the adsorbed phase, whereas at high surface coverage, the adsorbate–adsorbate interactions are dominant in shaping the thermodynamic properties.

Mamora and Seo[59] conducted an experiment to evaluate the feasibility of displacing natural gas with CO_2 within a carbonate sample. Experiments were conducted at varying temperatures and pressures. The results showed that over 70% of the gas can be recovered through the injection of CO_2. The study was restricted to only methane recovery and horizontal displacement. In reality, one must also consider the effect of gravity as it would affect displacement stability and subsequently recovery of natural gas.

Eliebid *et al.*[60] studied the effect of injecting CO_2 in pink desert limestone for the purposes of enhanced gas recovery. Competitive adsorption of CO_2 and CH_4 was studied at various temperatures. The adsorption-desorption experiments showed that CO_2 injections strongly affected natural gas desorption from the rocks as limestone has greater selectivity towards CO_2. As such, the CO_2 will compete with the CH_4 for the adsorption sites and reduce the adsorption of pure CH_4. Additionally, it was found that at lower temperature, greater amount of CO_2 can be stored in the rock sample.

2.2 Molecular Dynamics Simulation

Another approach to better understanding the properties of these CO_2 and *n*-alkane mixtures is through the use of molecular dynamic (MD) simulation. The basis of MD simulation is the integration of Newton's second law at a molecular level. This equation is given below:

$$m_i \frac{\partial^2 r_i}{\partial t^2} = F_i \quad \textbf{(1)}$$

Here r_i is the position of particle *i* and F_i is the force exerted on particle *i* of mass m_i. The force attributed to a certain particle can then be related to the potential energy (V) as follows[18]:

$$F_i = \frac{\partial V(r)}{\partial r_i} \quad \textbf{(2)}$$

By using these two equations it is possible to describe a system of defined particles, which when integrated can give the trajectory of the particles in time and space. The integration requires definition of initial velocities and position of particles. A key element of obtaining such trajectory is to be able to define the potential energy of each particle in the system. This is done by incorporating a potential energy function which will account for the dispersion forces. Examples of such functions include hard sphere, square-well, Lennard Jones and Kihara potentials among many others. One of the most commonly used potential functions is the Lennard-Jones potential (LJ)[30]. The appropriate potential function along with the relevant set of parameters is known as the forcefield. In other words, the potential energy is the sum of the intermolecular interactions from dispersion and electrostatic contributions, and intramolecular interactions from bonds, angle-bending and dihedral angle torsion and is given as follows:

$$V(r) = V_{non-bonded} + V_{bonds} + V_{angles} + V_{dihedral} \quad \textbf{(3)}$$

In general, there are several forcefields available in literature. These forcefields are of course relevant with respect to the system one is trying to simulate. For example, Le *et al.*[19]

simulated *n*-butane and CO_2/*n*-butane mixtures in 2 nm slit-like pores of silica. The forcefield used to describe the alkane and CO_2 was TraPPE-UA and the forcefield used to describe silica was CLAYFF forcefield. These simulations were carried out at various temperatures (subcritical to supercritical) as well as at various densities. The same authors have been involved with other works as well, which make use of the CLAYFF forcefield to simulate silica pores[19,20,21,27,49]. Phan *et al.*[20] simulated aqueous methane mixtures in silica pores. The solid substrate was obtained from b-cristobalite. The solubility of methane in water in confined spaces vs. in bulk conditions was measured, and it was found that the solubility of methane in water in confined spaces is much greater. The forcefield used to describe silica was also the CLAYFF forcefield. Ho *et al.*[21] tried to explore the properties of water at liquid–solid interfaces with the solid being silica. In that work, two different types of forcefields were used to simulate silica, which were CLAYFF and 'Brodka and Zerda' forcefields[50]. Silica described by the CLAYFF forcefield tended to attract water more strongly than the others. Cygan *et al.*[22] developed CLAYFF which is a general forcefield for simulation of hydrated and multicomponent mineral systems and their interfaces with aqueous solutions. It makes use of a harmonic relationship to describe bond stretch energy and the bend energy.

Emami *et al.*[23] described a forcefield for silica with a choice for functional form. Such functional forms can be used can be categorized into 2 sets. The first set of equations corresponds to CHARMM, CVFF and AMBER and the second set corresponds to PCFF and COMPASS forcefields. The difference between these two sets is the use of 12–6 LJ potential in the former and 9–6 LJ potential in the later for repulsive and dispersive van der Waals interaction. The bonded parameters follow a harmonic relationship. Cruz-Chu *et al.*[24] produced a forcefield for silica that is good for reproducing wetting properties of silica surfaces with different concentration of silanol

(Si-O-H) groups and is applicable to confined environments consisting of silica topography. The forcefields used to describe silica in the work of Cruz-Chu *et al*. were GLASSFF_2.01 and GLASSFF_1.01. Duin *et al.*[25] developed a forcefield to predict the structure, properties and chemistry of materials involving silicon and silicon oxides. The ReaxFFSiO forcefield is based on ReaxFFCH, which is for hydrocarbons and hence is good for reaction of organic components with Si or SiO_2 systems. The forcefield is specifically developed for systems where hydrocarbons are undergoing a reaction.

Previously, studies relating to the effect of confinement on various fluids have been carried out using MD simulations. Santos *et al*.[26] studied the behavior of a CO_2 and *n*-alkane mixture within a calcite nanopore. It was shown that CO_2 is able to replace hydrocarbons that are adsorbed on to the calcite substrate and the number of adsorption sites on the calcite surface determine the amount of CO_2 that is adsorbed. Furthermore, it was concluded that the temperature, pore size, concentration of CO_2 in the system, and the length of the hydrocarbon chain all play a vital role in the preferential adsorption of CO_2 over the hydrocarbon. The results validated experimental evidence of higher adsorption selectivity of CO_2 over alkanes. Higher temperature caused the CO_2 and alkanes to accumulate in the center of the pore and the amount of molecules that adsorbed on to the calcite wall decreased. It was also found that medium to long chain alkanes aligned onto the substrate, in a parallel configuration and the dihedral distribution is independent of effect of confinement. In general, the paper validated experimental evidence on the ability of CO_2 to enhance oil or gas recovery.

Bui *et al*.[27] studied the transport properties of methane within water-filled nanopores made out of different materials: silica, magnesium oxide, muscovite, alumina and calcite. It was concluded that the diffusion of methane within the water-filled nanopores was strongly affected

by the type of solid substrate that made the pore. The parallel self-diffusion coefficient was found to be isotropic for all the substrates studied except for calcite where it was found to be anisotropic. This was attributed to the heterogeneous water distribution in the different hydration layers as well as the low free energy pathways. In general, the local molecular properties of water under confinement, molecular structure and the solvation free energy all played a major role in affecting the self-diffusion of methane. The results require experimental validation but if proven true, provide a strong case for the applications of gas separation as well as successful recovery of shale gas through tertiary recovery means.

Wang *et al*. [28] studied the effect of pressure, moisture content and different mineral types on diffusion of methane. The results showed that the methane diffused much faster as the pore size and temperature increased or as the pressure decreased. Moisture was found to negatively affect the diffusion of methane inside organic pores, as the water formed a cluster. In inorganic pores however, water only forms a thin adsorbed layer onto the surface of the pore, and as such does not have a strong impact on the diffusivity of methane. In general, it was deduced that CH_4 adsorption is the highest in pores made out of organic material and lower in pores made out of inorganic materials, such as within calcite. The work proved molecular dynamics to be a complimentary tool to experiments as experimentation is not always feasible. Furthermore, it provided greater insight on hydrocarbon transport within shale pores of different materials.

Molecular dynamics simulations have also been conducted to understand the interfacial properties of *n*-decane/CO_2 mixture within confinement[29]. A binary system of *n*-decane and CO_2 in silica nanopore was studied at different pressures. The diffusivity of *n*-decane was found to increase upon the injection of CO_2 in the pore. However, an excess addition of CO_2 in the system caused the overall diffusivity of the hydrocarbon and CO_2 to decrease. The parallel self-diffusion

coefficient was found to be much greater than the perpendicular self-diffusion co-efficient. The non-monotonous change in the diffusivity of *n*-decane can be attributed to the differing trends in the different zones within the system (i.e. dense layer and central layer), as well as the amount of *n*-decane displaced into the middle of the pore. The work provides great insight of the importance of using an optimal amount of CO_2 in the application of enhanced oil / gas recovery as it will affect economic feasibility as well as efficiency. Molecular dynamics has proven to be an important tool that can allow one to obtain equilibrium and transport properties which are of special interest, especially when trying to understand EOR/EGR, and act as a precursor or substitute to experiments which can be costly and time-consuming.

In most of these works, diffusion is an important transport property of interest. However, most of the work related around diffusion has been through the use of mean square displacement on the basis of the Einstein relation. In the case of a homogenous system, the diffusion coefficient of a fluid is the same in any direction (x, y and z). In such case, the Einstein relation can be used to calculate the self-diffusion coefficients. However, in the case of confinement, the system is inhomogeneous and the diffusion coefficients in different directions would be different. As such, understanding as well as being able to calculate these varying diffusion coefficients is vital to comprehending how a fluid would behave in confinement. If the slit pore has two slabs orthogonal in the z direction, then the mean force potential would only be exhibited in the z direction. Hence, one would expect a different diffusion coefficient in the z direction (perpendicular self-diffusion co-efficient) and in the x and y direction (parallel self-diffusion coefficient) [51]. If the slabs of the slit pore are isotropic on a molecular level, then the self-diffusion coefficients in the x and y direction would be the same.

2.3 Equations of State

Equations of state (EOS) can also be used to study the effect of confinement. The effect of confinement can be represented using the statistical mechanical representation of Helmholtz energy expressions which lead to the development of relevant EOS. Various EOS such as van der Waals, Redlich–Kwong, Soave–Redlich–Kwong, and Peng–Robinson have been applied to systems involving cylindrical and spherical pores[61,62]. Tan *et al.*[62] integrated the perturbed-chain statistical associating fluid theory (PC-SAFT EOS) with the Young – Laplace equations to explore phase equilibrium within cylindrical pores.

These models come with their advantages and disadvantaged. For example, if the pore size is large enough and the effect of the wall is negligible, one can assume that the fluid in the system would behave as a bulk fluid. These models are convenient from this perspective, as they would give comparable results to using a model solely developed for bulk fluids. A disadvantage however, of using such models is that they are unable to evaluate the local distribution of the fluid within the pore. An approach to overcome such a disadvantage was used by Dawass *et al.*[63] who used the multipotential theory of adsorption (MPTA). Dawass *et al.* developed a general formulation that not only accounts for different potentials owing to different type of substrates but also different external fields such as gravitational, electrical, and magnetic. The above work allowed for the prediction of local composition profiles for fluids under confinement, with a lower computational load than when compared to molecular simulations, however, at a much coarser level.

CHAPTER III

METHODOLOGY

3.1 General Simulation Details

The focus of this study is to understand the behavioral changes of pure hydrocarbons and their mixtures with CO_2, with respect to their properties within confinement in various substrates. Both long chain and short chain hydrocarbons were studied. The systems were simulated using Groningen Machine for Chemical Solutions (GROMACS 4.6.5.)[31]. All the systems were simulated in a canonical (NVT) ensemble. An illustration of an NVT ensemble is shown in Figure 1. Since this study is focused on the effect of confinement, and pore size is a parameter, it is important to keep the pore size fixed which is achievable by using an NVT ensemble. Similarly, the same ensemble allows one to keep the number of molecules and temperature constant within the simulation box. Hence, if one were to take a snapshot of the system at different times, different configurations and positioning of the same number of molecules will be observed in the same space, and at the same temperature. The leapfrog algorithm was used to integrate Newton's equations of motion and a time-step of 0.001 picoseconds was used in most simulations. However, when studying the effect of different substrates, a time-step of 10 picoseconds was used. Nose – Hoover thermocouple was used to control the temperature within the simulations. Periodic boundary conditions were applied in the *x*, *y* and *z* direction to obtain a slit-shaped pore with infinite surface area. The cut-off radius was kept at 1.4 nm and the Particle Mesh Ewald (PME) summation method was used to account for long range electrostatic interactions. The simulation time varied based on the system. Less complex systems or systems which involved small chain *n*-alkanes such as methane were run for 30 ns as it was enough time to reach equilibrium. More

complex systems or systems that involved long chain *n*-alkanes such as *n*-decane were run for 50 to 60 ns. In all cases, the last 3 ns were used for post processing.

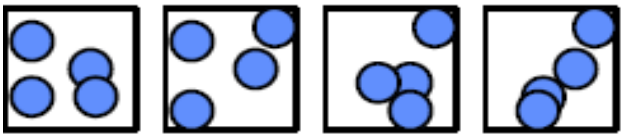

Figure 1: Canonical Ensemble is a closed isothermal system, i.e. constant number of molecules, volume and temperature. Different boxes represent different configurations and different times

3.2 Fluid Model Development

The alkanes (Methane, ethane, *n*-Octane and *n*-decane) and CO_2 studied in the systems, were all described using the TraPPE (Transferable Potentials for Phase Equilibria) forcefield[32,33]. The TraPPE forcefield uses 12-6 Lennard Jones Potential and the coulombic interactions to describe the dispersion and the electrostatic forces between atoms that are separated by three bonds or are part of a different molecule and is described as follows:

$$u(r_{ij}) = 4\epsilon_{ij}\left[\left(\frac{\sigma_{ij}}{r_{ij}}\right)^{12} - \left(\frac{\sigma_{ij}}{r_{ij}}\right)^{6}\right] + \frac{e^2}{4\pi\varepsilon_0}\frac{q_i q_j}{r_{ij}} \quad \textbf{(4)}$$

where r_{ij} represents the separation between the atoms, ϵ_{ij} represents the well depth, σ_{ij} represents the size respectively for the pair of atoms, q_i and q_j represent the partial charges on atoms *i* and *j*, and ε_0 represents the vacuum permittivity. The parameters used are given in Table 1. Furthermore, TraPPE constraints the bond length at 0.154 nm and the harmonic potential is used to describe the bond angle bending and the OPLS united atom torsional potential[34] is used to describe the dihedral angle motion for large-chain hydrocarbons. Both are given as follows:

$$u_{bend} = k_\theta(\theta - \theta_0)^2/2 \quad \textbf{(5)}$$

$$u_{tors} = c_1[1 + \cos(\varphi)] + c_2[1 - \cos(2\varphi)] + c_3[1 + \cos(3\varphi)] \quad \textbf{(6)}$$

Where k_θ is the force constant and is given by $62500k_B$, k_B is the Boltzmann Constant[5], θ_0 is 114° and $\frac{c_1}{k_B} = 355.03\ K, \frac{c_2}{k_B} = -68.19\ K$ and $\frac{c_3}{k_B} = 791.32\ K$. Finally, the Lorentz – Berthelot combining rules were used to take into account interactions between unlike atoms[35,36]:

$$\sigma_{ij} = (\sigma_{ii} + \sigma_{jj})/2 \quad \textbf{(7)}$$

$$\epsilon_{ij} = \sqrt{\epsilon_{ii}\epsilon_{jj}} \quad \textbf{(8)}$$

Table 1. Lennard Jones Parameters for TRaPPE Forcefield. Adapted from [32, 33]

Component	$\boldsymbol{\sigma}$ $(\boldsymbol{m})$	$\boldsymbol{\epsilon}$ $(\boldsymbol{kJ/mol})$	$\boldsymbol{q}(\boldsymbol{e})$
CH_4	3.73×10^{-10}	1.231	0.00
CH_3	3.75×10^{-10}	0.814	0.00
CH_2	3.95×10^{-10}	0.814	0.00
C (C in CO_2)	2.80×10^{-10}	0.240	0.70
O (O in CO_2)	3.05×10^{-10}	0.687	-0.35

A range of densities were studied from 50 kg/m^3 to 350 kg/m^3 for short chain hydrocarbons and 450 kg/m^3 to 650 kg/m^3 for long chain hydrocarbons and their mixtures. The molecules were

initially randomly placed within the slit-shapes pores. Figure 2 shows a snapshot of the initial configuration of CH_4 and CO_2 in a 4 nm silica pore.

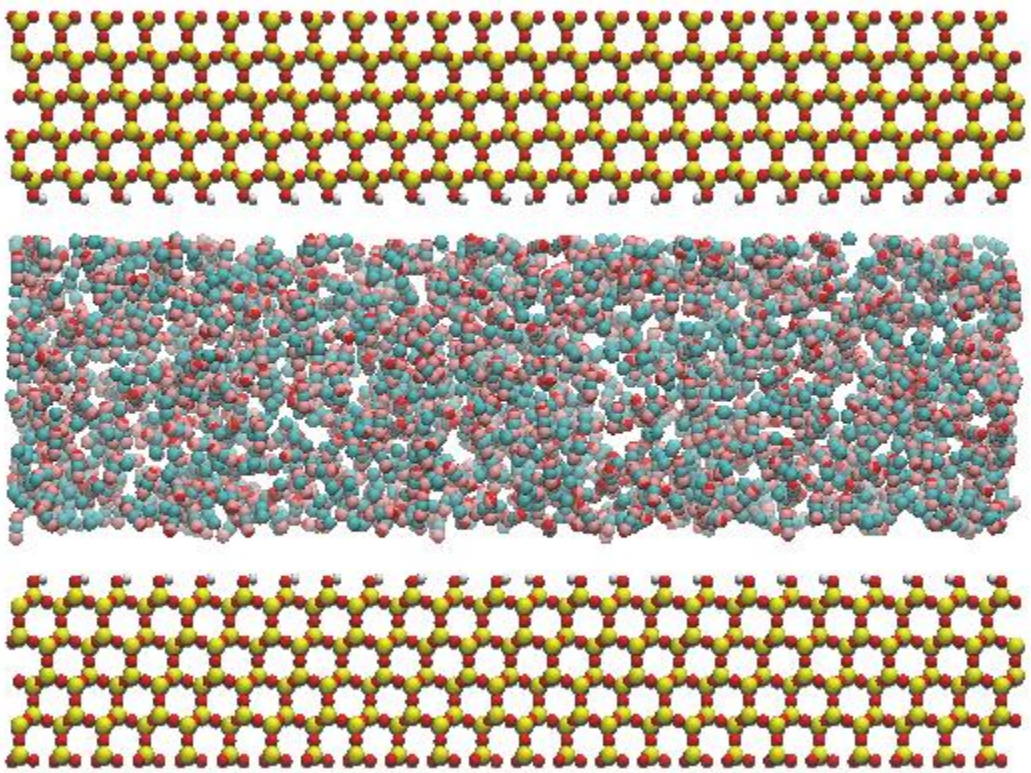

Figure 2: Sample Initial Configuration: Methane and Carbon Dioxide in 4nm Silica Pore, Fluid Density: 300 Kg/m^3

3.3 Substrate Model Development

The majority of the simulations have been conducted with a pore made out of silica. However, different substrates such as calcite, muscovite, alumina and magnesium oxide were also studied. The ClayFF[22] forcefield was used for all substrates except calcite. For calcite, the forcefield proposed by Xiao *et al.*[37] was used.

The ClayFF forcefield uses a similar set of equations as TraPPE to describe the various substrates. The only difference is that the bond length is not fixed at a specific value but its contribution to the potential energy is given by the following expression:

$$u_{bond} = k_1(r_{ij} - r_0) \quad \textbf{(9)}$$

The parameter details for the ClayFF forcefield separately identifies oxygen atoms that bond with the metal ion of the substrate, essentially forming a bridge between 2 metal ions (bridging oxygen), and oxygen atoms that is bonded to a metal ion and another ion which causes the substrate to be capped off (non-bridging oxygen). Thus, non-bridging oxygen atoms will be found towards the surface of the wall. The parameters for this forcefield are found in Tables 2,3 and 4.

Table 2. Non-Bonded Parameters for ClayFF Forcefield. Adapted from [22]

Component	$\boldsymbol{\sigma}$ $(\boldsymbol{m})$	$\boldsymbol{\epsilon}$ $(\boldsymbol{kJ/mol})$	$\boldsymbol{q}(\boldsymbol{e})$
Si	$3.30\text{x}10^{-10}$	$7.70\text{x}10^{-6}$	2.10
Al	$4.27\text{x}10^{-10}$	$5.56\text{x}10^{-6}$	1.58
Mg	$5.26\text{x}10^{-10}$	$3.78\text{x}10^{-6}$	1.05
K	$3.33\text{x}10^{-10}$	$4.18\text{x}10^{-1}$	1.00
O (Bridging)	$3.17\text{x}10^{-10}$	$6.50\text{x}10^{-1}$	-1.05
O (Bridging with Substitution)	$3.17\text{x}10^{-10}$	$6.50\text{x}10^{-1}$	-1.17
O (Non-bridging)	$3.17\text{x}10^{-10}$	$6.50\text{x}10^{-1}$	-0.95
H	0.00	0.00	0.43

Table 3. Bond Parameters for ClayFF Forcefield. Adapted from [22]

Bond Stretch		$r_0\ (m)$	$k_1\ (kJ/mol.m^2)$
Species i	**Species j**		
O (Non-bridging)	**H**	1.00×10^{-10}	4.63×10^{11}

Table 4. Angle Parameters for ClayFF Forcefield. Adapted from [22]

Bond Stretch			$\theta_0\ (rad)$	$k_\theta\ (kJ/mol.rad^2)$
Species i	**Species j**	**Species k**		
Metal	**O (Non-bridging)**	**H**	1.91	251.04

Xiao *et al.* has developed a forcefield for calcite for which the Lennard Jones parameters are given in table 5 and table 6 below:

Table 5. Lennard Jones Parameters for Calcite Forcefield. Adapted from [37]

Component	$\sigma\ (m)$	$\epsilon\ (kJ/mol)$	$q(e)$
Ca	2.96×10^{-14}	2.00	1.67
C_m	5.21×10^{-13}	3.69×10^{-1}	0.99
O_m	3.06×10^{-10}	1.32×10^{-7}	-0.89

Table 6. Pairwise Lennard Jones Parameters for Calcite Forcefield. Adapted from [37]

Component		$\sigma\ (m)$	$\epsilon\ (kJ/mol)$
Ca	**O_m**	inf	inf
C_m	**C_m**	5.37×10^{-15}	1.11×10^{-2}
O_m	**O_m**	4.89×10^{-13}	2.62×10^{-2}
O_m	**O_m**	1.90×10^{-12}	1.14×10^{-3}

The bond length between the carbon and the oxygen in the carbonate ion within the calcite structure was fixed at 0.118 nm. The parameters for the angle bending and the dihedral contributions are given as follows: $k_\theta/k_B = 2.228 \times 10^5\ K.rad^{-2},\ \theta_0 = 120,\ c_1/k_B = c_3/k_B = 0,\ c_2/k_B = 3477.1\ K$. The same methodology for developing the above substrates has previously been used in literature[20,21,38-43].

3.4 Self-Diffusion Coefficient Calculation Details

The self-diffusion coefficient can be calculated using two different approaches. The simplest approach is to calculate the perpendicular and parallel self-diffusion coefficients. This approach uses Einstein method of relating the self-diffusion coefficient to the mean square displacement of the particle. The self-diffusion coefficient according to this method is given as:

$$D = \frac{1}{2d} \lim_{t \to \infty} \frac{\langle \Delta r^2(t) \rangle}{t} \quad \textbf{(10)}$$

Where D is the self-diffusion coefficient, d is the dimension of the system, $\langle \Delta r^2(t) \rangle$ is the mean square displacement, and t is the time.

This method to calculate self-diffusion coefficient does not take into account any heterogeneity of the system. As such, it is not the most accurate method to calculate the self-diffusion coefficient of various components within the system due to the heterogeneity inducing effect of confinement. This is so because the confinement causes the creation of a denser layer of fluid towards the wall and a less dense layer of the fluid towards the middle of the pore.

The second approach is to calculate the parallel and perpendicular self-diffusion coefficient based on different regions. Thus, separately for the dense layer near the wall and the less dense layer towards the center of the pore respectively. To calculate the parallel self-diffusion coefficient, an approach developed by Liu *et al*.[44] and explored by Franco *et al*.[45] can be used that calculates the self-diffusivity specific to the region. It is summarized by the following equation:

$$D_{\parallel} = \lim_{t \to \infty} \frac{\langle \Delta r^2(t) \rangle_{\Omega}}{2tP(t)} \quad \textbf{(11)}$$

Where $D_{||}$ is the parallel self-diffusion coefficient, $\langle \Delta r^2(t) \rangle_{\Omega}$ is the mean square displacement across the distance interval Ω and $P(t)$ is the survival probability, which is given as follows:

$$P(t) = \frac{1}{\tau} \sum_{t_0}^{\tau-1} \frac{N(t_0, t_0 + t)}{N(t_0)} \quad \textbf{(12)}$$

Here, $N(t_0 + t)$ is the total number of centers of mass within the interval Ω at $t_0 + t$. $N(t_0)$ is the total number of centers of mass within the interval Ω at t_0. The perpendicular self-diffusion coefficient in the different regions can be calculated using the approach highlighted by Franco *et*

al.[45] which requires the calculation of residence time obtained from integration of the survival probability expression:

$$\tau_r = \int_0^\infty P(t)\,\mathrm{d}t \tag{13}$$

The perpendicular self-diffusion coefficient is then calculated as:

$$D_\perp = \frac{L^2}{\alpha\tau_r} \tag{14}$$

$$\alpha^{-1} = 4\omega L\frac{(e^{wL}+1)}{(e^{wL}-1)}\sum_{j=0}^{\infty}\left[(2j+1)^4\pi^4 + \frac{3\omega^2L^2}{4}(2j+1)^2\pi^2 - \frac{\omega^4L^4}{4}\right]^{-1} \tag{15}$$

where ω is the positive slope of the equation that represents the peak of the component of interest in the density profile.

3.5 Orientation Analysis

This study also includes the effect of confinement on the orientation of the fluid. The approach developed by Santos *et al*.[26] was used to conduct this analysis. The angle between the end-to-end vector and the vector perpendicular to the substrate was calculated. An angle of 0º or 180º represents a perpendicular orientation, whereas an angle of 90º represents a parallel orientation of the component in relation to the mineral surface. The dihedral distribution of the fluid components within the confinement was calculated and compared to their dihedral distribution profile in bulk. The last 3 nanoseconds of the simulations were used for this analysis.

3.6 Equation of State Methodology

The methodology used in this work is the same as that adopted by Dawass *et al.*[63]. The method involves the use of canonical ensemble. Because of that, the inputs given to the system are the volume of the pore, the system temperature as well as the number of molecules of each component type. Minimizing the Helmholtz energy of the system will result in obtaining the equilibrium conditions. The Helmholtz energy of the system is simply the summation of the Helmholtz energy in the different regions, but integration is done over each region to obtain an accurate representation of Helmholtz energy contribution due to the heterogeneity of the regions. The equation of state used by Dawass *et al.* in her work is Peng – Robinson. The SAFT – VR Mie EOS has been implemented in this work. This method has a clear underlying set of assumptions, which are as follows:

1. The temperature, number of molecules and the volume of the system is known and is a constant
2. The system is broken down into different regions depending on the number of external fields applied; the volume of each system is known and is a constant
3. The heterogeneity is accounted for by integrating the Helmholtz energy across each region. Each region can be divided into discrete grid elements
4. The effect of confinement is completely captured by the interaction potential between the wall and the fluid molecules

CHAPTER IV

RESULTS AND DISCUSSION

4.1 Validation of Forcefield

Over the course of this work, multiple forcefields have been used to describe various fluids and substrates. The forcefields have readily been validated in the literature[22,31-33]. However, for assurance, this section will provide brief evidence on forcefield validity using a few examples. Hence, isotherms were plotted for *n*-alkanes (methane, ethane, propane and *n*-butane). These isotherms were obtained at a temperature of 250 K and 500 K and the results were compared to data from National Institute of Standards and Technology (NIST) database[46]. The results obtained from the simulations were quite comparable to the data from NIST at lower temperature and higher pressure. The simulation data was most accurate with respect to NIST data. These results are shown in Figure 3.

Furthermore, dihedral angle distribution of *n*-butane was obtained to ensure appropriate representation of a real fluid by the force fields used in this work and is shown in Figure 4. The larger central peak in these curves represent the *Trans* minima of the potential, whereas the smaller peaks on the sides represent the *Gauche* minima of the potential. The results obtained for *n*-butane match quite well with what is available in literature[47,48]. In fact, integrating the curves to obtain the *Trans* and *Gauche* populations yield numerical values of 70% and 30% respectively. These values compare quite well to data available in a previous simulation study[47] (*Trans* population reported as 67.8%) as well as data from Raman scattering[48] (*Trans* population reported as 70.7%).

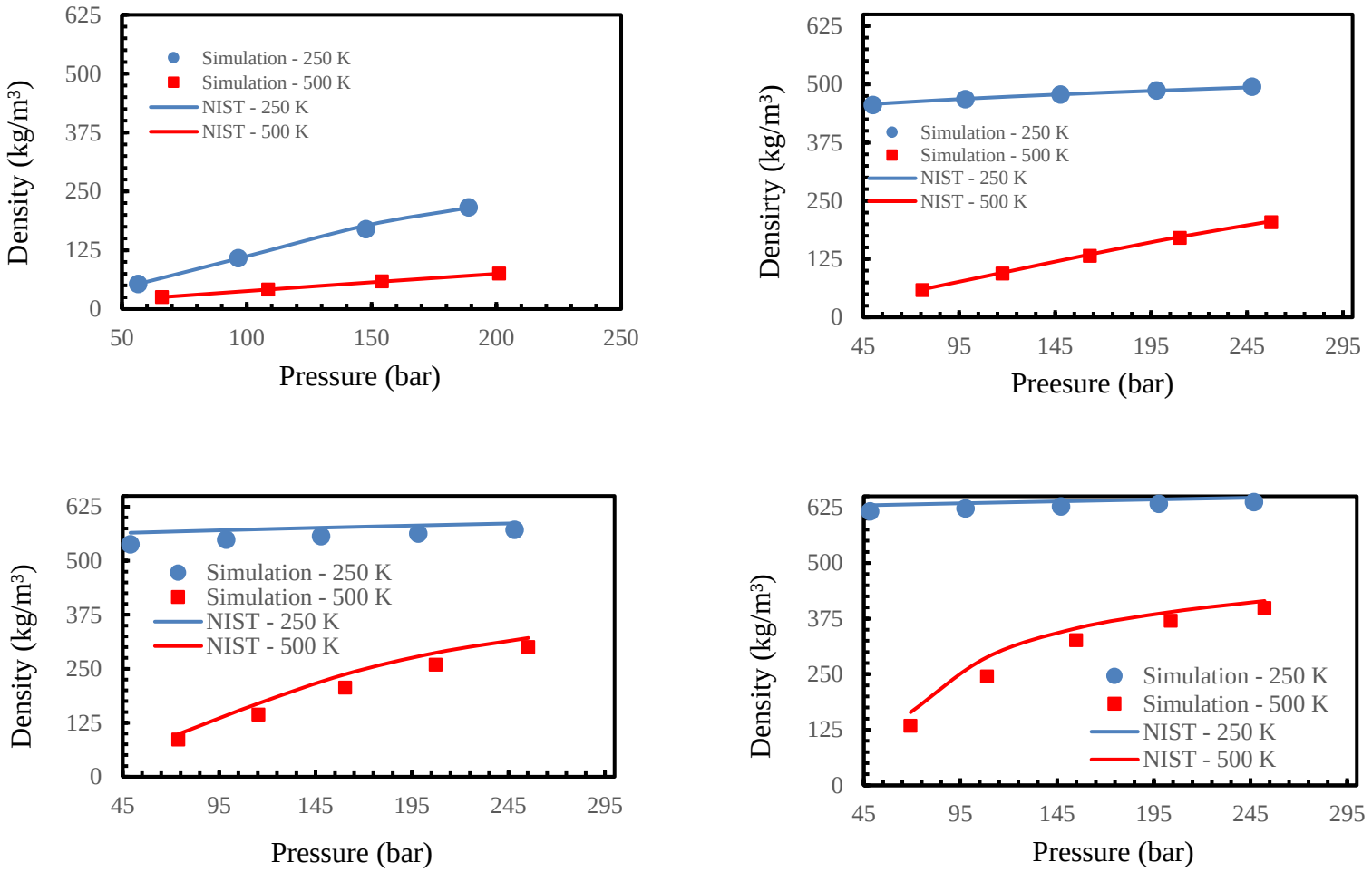

Figure 3: Isotherms: Top Left) Methane, Top Right) ethane, Bottom Left) propane, Bottom Right) *n*-butane. Isotherms plotted at 250 K and 500 K

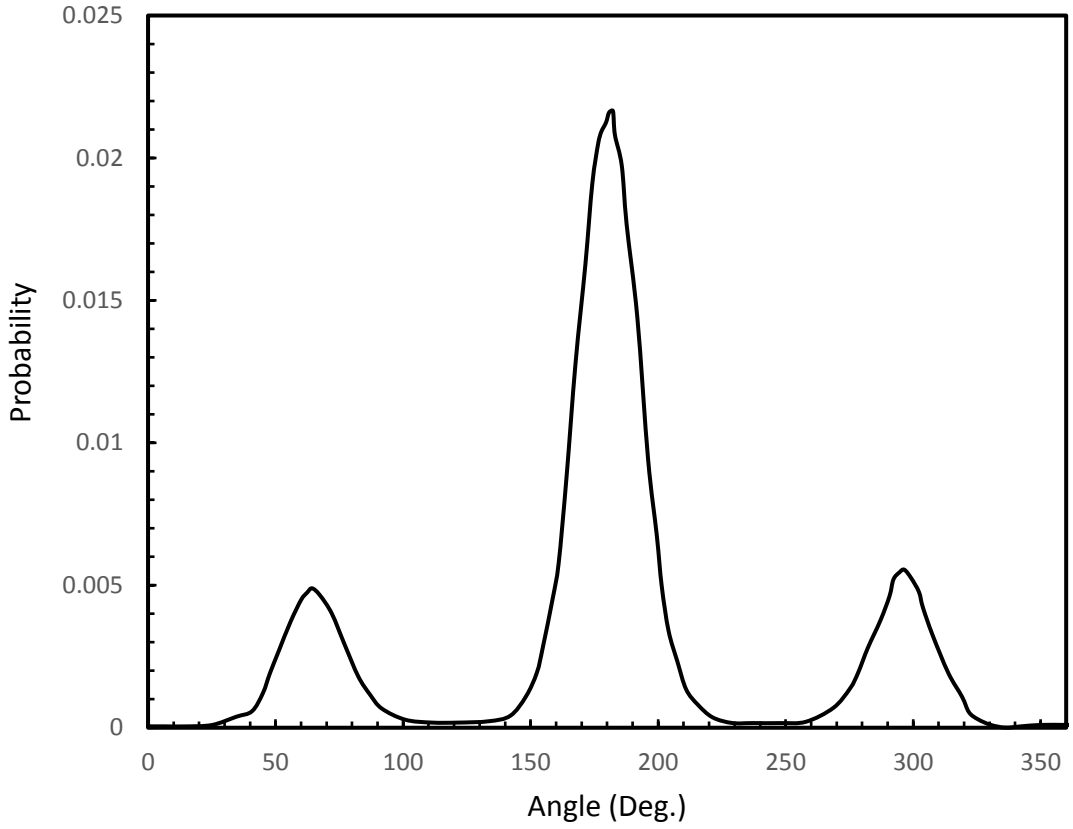

Figure 4: Dihedral Angle Distribution of *n*-butane at 300 K

4.2 General Characteristics of n-alkane and CO2 System in Silica

A study was conducted to understand the behavior of long chain hydrocarbons in confinement within silica along with CO_2. Figures 5 and 6 show the density profiles of CO_2 – *n*-octane and CO_2 – *n*-decane at different mixture densities respectively, with mole fraction of the CO_2 being 0.67, and at a temperature of 375 K within a silica nanopore of 4 nm. A similar simulation has been conducted by Santos *et al.*[26] where a system consisting of *n*-octane and CO_2 with a calcite pore of 4 nm was studied. The results reported by Santos *et al.* showed that the hydrocarbon was pushed to the middle of the pore whereas CO_2 travelled towards the pore walls due to the affinity between CO_2 and the molecules of the wall. A similar trend is noticed in the case of *n*-octane and *n*-decane as evidenced by Figures 5 and 6. Comparing Figure 4 to the results shown by Santos *et al.* the affinity of CO_2 towards calcite is much stronger compared to silica. The effect of pore material will be explored in section 4.6.

As the amount of CO_2 present in the system increases, *n*-octane and *n*-decane are further pushed towards the center of the pore. There are several points of interests to be noted in Figures 5 and 6. Firstly, as the mixture density increases, the *n*-alkane density at the center of the pore increases. Furthermore, near the wall, *n*-alkane has already reached saturation at the lowest mixture density (450 kg/m^3) simulated. This is evidenced by the fact that as the mixture density increases, the *n*-alkane density increases in the center of the pore but the height of the peaks on each side of the curve remain constant.

Contrary to that, CO_2 has still not reached saturation in the adsorbed layer. This can be seen by the peaks on the side of the curve, in Figures 5 and 6, which continue to increase in height, indicating that the density of CO_2 in the dense layer is increasing as there is an increase the density. Thus, there are still active sites present on the substrate for CO_2 to adsorb on to. As the density of

the mixture is increased, there are more CO_2 molecules in the system and thus greater number of CO_2 molecules adsorb onto the surface of the silica, thus increasing the peak as seen on the curve. As the majority of the CO_2 molecules get adsorbed onto the surface, only small increases in the density of CO_2, at the center of the pore, can be seen. Comparing this to *n*-alkane, it can be seen that the density at the center of the pore increases at a greater increment with increase in mixture density.

Injecting CO_2 into the pore, as proved in literature and in this work, is effective in improving the mobility of the hydrocarbon. If only hydrocarbon would be present inside the pore without the absence of CO_2, it would be much more adsorbed onto the walls of the pore and the overall mobility of the hydrocarbon would lessen. An example of this is in the work of Le *et al.*[19] who showed the density profile of pure butane within a 2 nm silica pore. The same system was simulated in this work and compared to the results published by the author, shown in Figure 7.

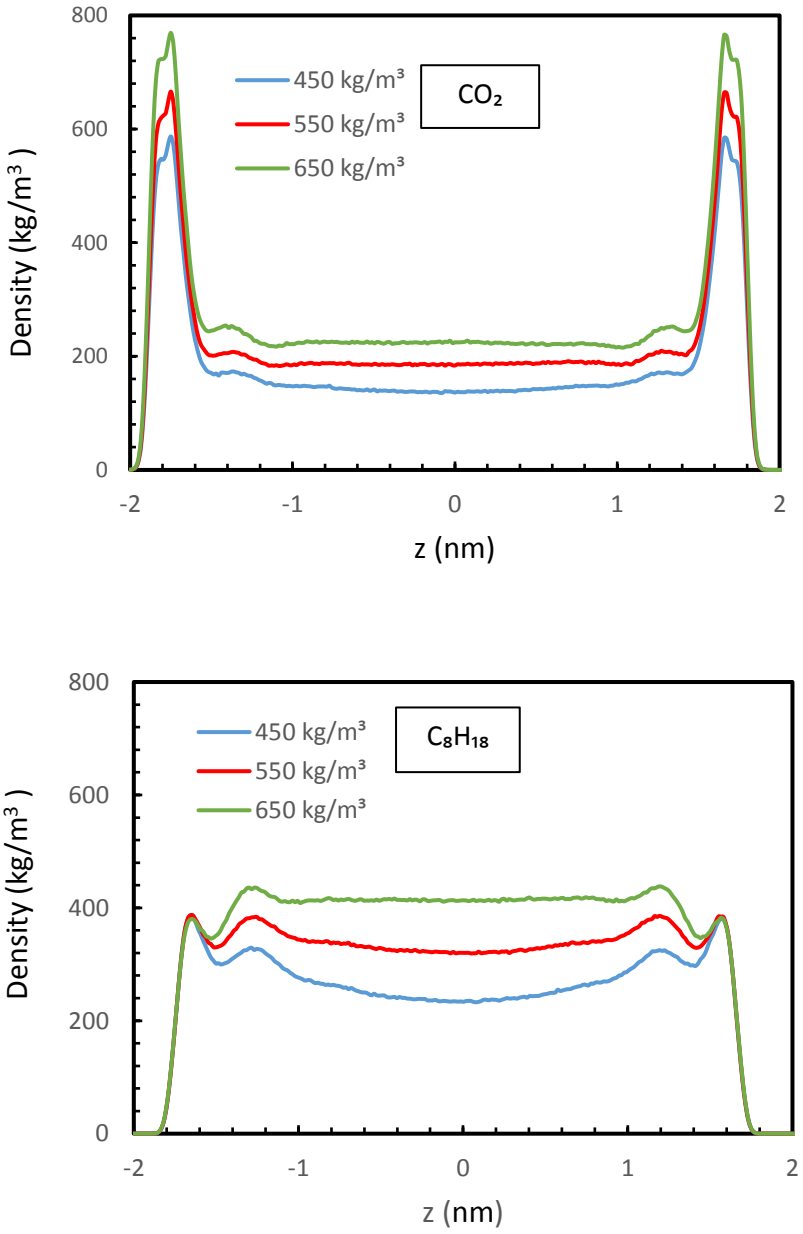

Figure 5: Density Profiles: Top) CO_2 (blue: 450 kg/m^3 mixture density, red: 550 kg/m^3 mixture density, green: 650 kg/m^3 mixture density. Bottom) *n*-octane (blue: 450 kg/m^3 mixture density, red: 550 kg/m^3 mixture density, green: 650 kg/m^3 mixture density),

.

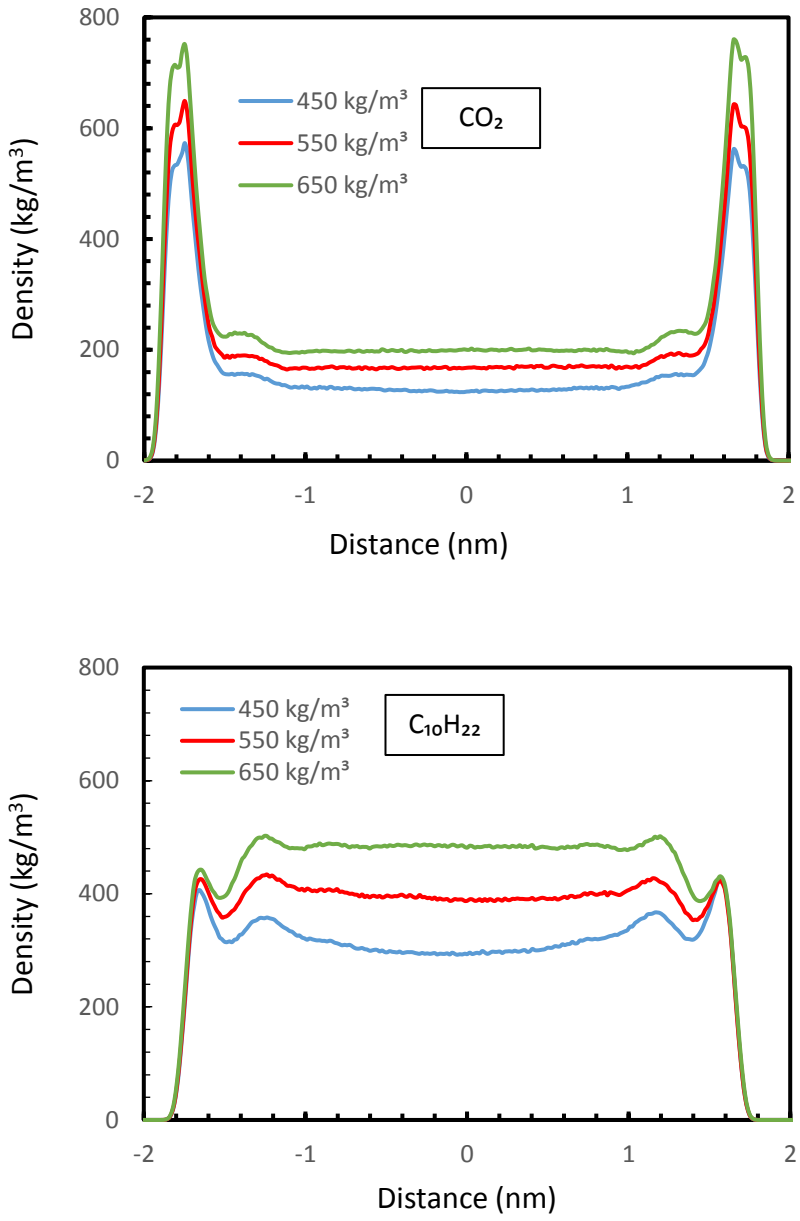

Figure 6: Density Profiles: Top) CO_2 (blue: 450 kg/m^3 mixture density, red: 550 kg/m^3 mixture density, green: 650 kg/m^3 mixture density**,** Bottom) *n*-decane (blue: 450 kg/m^3 mixture density, red: 550 kg/m^3 mixture density, green: 650 kg/m^3 mixture density)

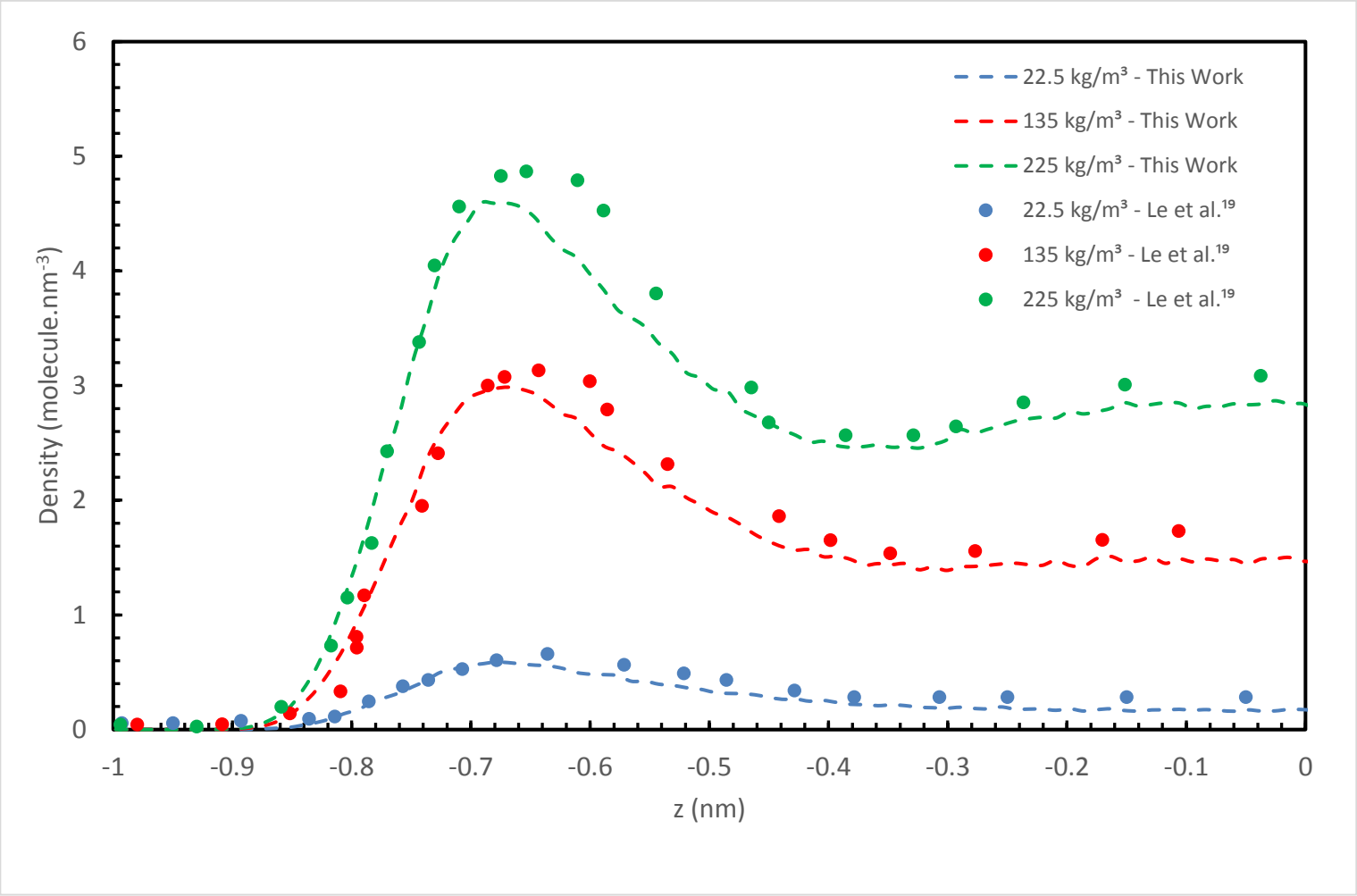

Figure 7: Density Profiles of Butane in a 2 nm Silica Pore at Three different Densities

4.3 Effect of Mixture Density

The effect of changing mixture density was measured in a system containing methane and CO_2 within a 4nm silica pore at 375 K in a molar ratio of 1:1. Mixtures of densities varying from 50 kg/m^3 to 300 kg/m^3 were examined. As shown in Figure 8, one would expect that with the increase in density of the mixture, almost all the extra methane that comes with increasing the mixture density is pushed to the center the pore due to the affinity of CO_2 to the substrate and thus more readily occupying the active sites.

Unlike in the case of *n*-decane, where a saturation in terms of *n*-decane adsorbing on the active sites was observed, the amount of methane that can be adsorbed onto the substrate here has not reached a saturation point and there are still some active sites available for methane to adsorb on to. This can be deduced from the fact that the peaks of *n*-decane density profile do not change upon increase in fluid density but the peaks of methane density profile do exhibit the slight shift in height as the density is increased. This could be due to the fact that the methane molecule has a much lower molecular weight compared to *n*-decane, making the former easily adsorbed onto the active sites. Another important point to mention is that, Striolo *et al.*[49] and Santos *et. al*[26]. had shown that the *n*-octane molecules adsorb onto the surface, within confinement, in a parallel fashion. This is something that has been tested and validated within this work as well. A similar trend of *n*-decane adsorbing in a parallel fashion on to the wall can be calculated. This means that a longer *n*-alkane either requires more than one active site to be properly adsorbed or, if it uses only one active site, due to the nature with which an *n*-decane molecule places itself onto the wall, it may cause certain active sites to be blocked. Another more trivial reason for *n*-decane reaching saturation as opposed to methane can be attributed to the fact that in the study explained previously, more *n*-decane molecules were present compared to the methane molecules.

As such, it is observed that increasing the density is causing the peaks to slightly increase as more methane molecules are available for adsorption. The curves pertaining to CO_2 show a much greater increase in peaks as the density increases compared to the increase in the center of the pore. However, the increment in height of the peaks decreases for CO_2 as well since an increase in density means a greater number of molecules in the same space while the number of adsorption sites remain the same. This fact is reflected in Figure 9. It can be seen that as the fluid density is increasing, the curve representing the amount of CO_2 being adsorbed onto the surface, although still increasing, is plateauing as well. Whether the amount of CO_2 adsorbed per unit area reaches the same value as the amount of adsorption sites per unit area may very well depend upon the orientation that CO_2 prefers. A parallel orientation to the surface may result in the CO_2 being adsorbed onto two active sites, due to the interaction between the H atom of the hydroxyl group of the silica and the two O atoms of CO_2, indicating that CO_2 may need two active sites. Similarly, a perpendicular orientation may result in CO_2 only occupying one active site.

Increasing the density also decreases the perpendicular self-diffusion coefficient both at the center of the pore and in the dense layer. The results for perpendicular self-diffusion coefficient are shown in Figure 10. The center of the pore was considered to be 2.8nm to 4.8 nm and the dense layer varies depending on the density profiles. The decrease in the diffusion can be attributed to the fact that increasing density means that there is a greater steric hindrance and a greater amount of collisions among the molecules. This factor considerably affects the diffusivity of the components within the fluid. A similar qualitative trend has been reported by Le *et al.*[19] for a binary mixture of butane and carbon dioxide within silica. For all generated data on perpendicular self-diffusion coefficient, it was found that the error bars were negligible compared to the true value. As such, even though present on the plots, they are difficult to see. Error bars were calculated by

allowing the simulations to run for a further 10 ns after equilibrium was reached. Block analysis was conducted on these 10 ns by splitting them into 2.5 ns each. This is the methodology that has been largely used across similar types of work in literature[19, 41, 49, 51]. As such, it would seem that the system is sensitive to the initial configuration and it would be interesting to measure the size of the error bars from running different runs of the same system with different initial configuration.

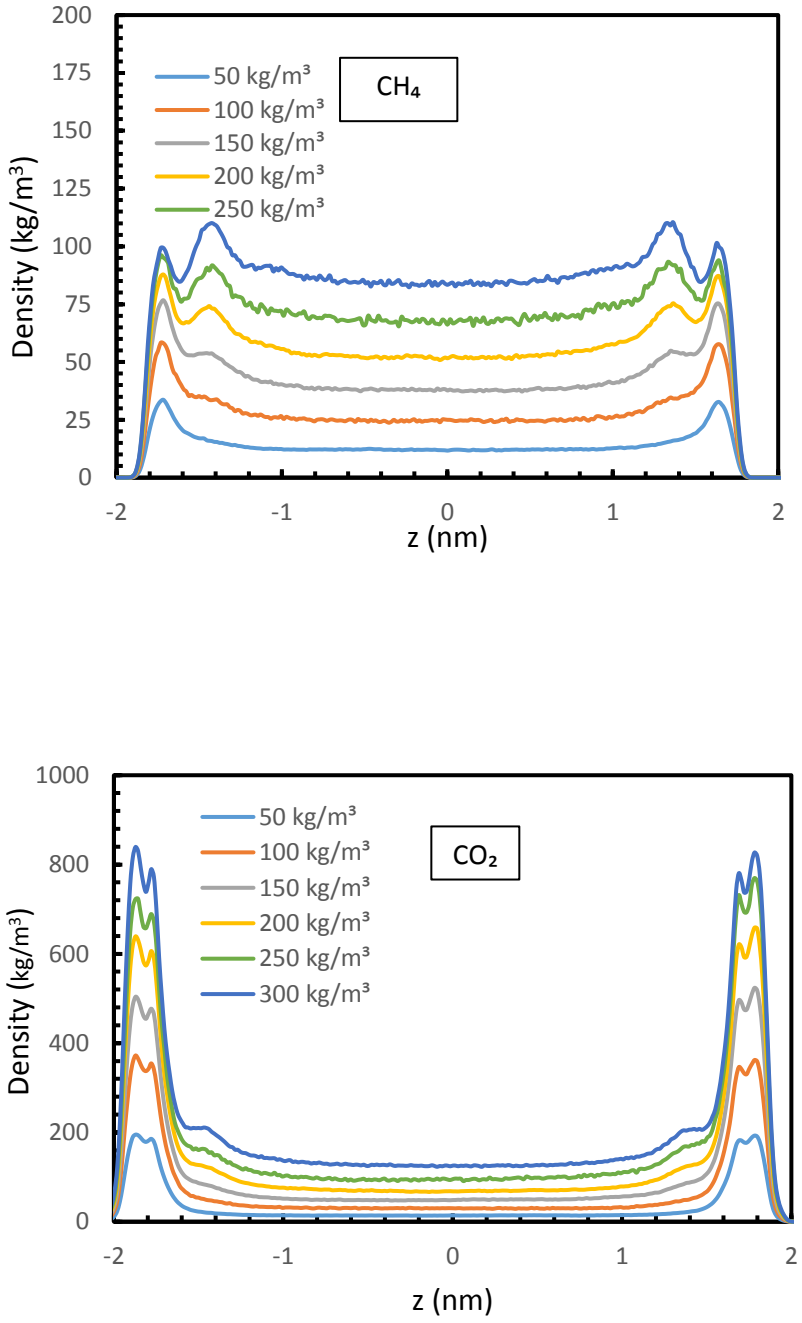

Figure 8: Density Profiles: Top) Methane at different mixture densities and Bottom) CO_2 at different mixture densities

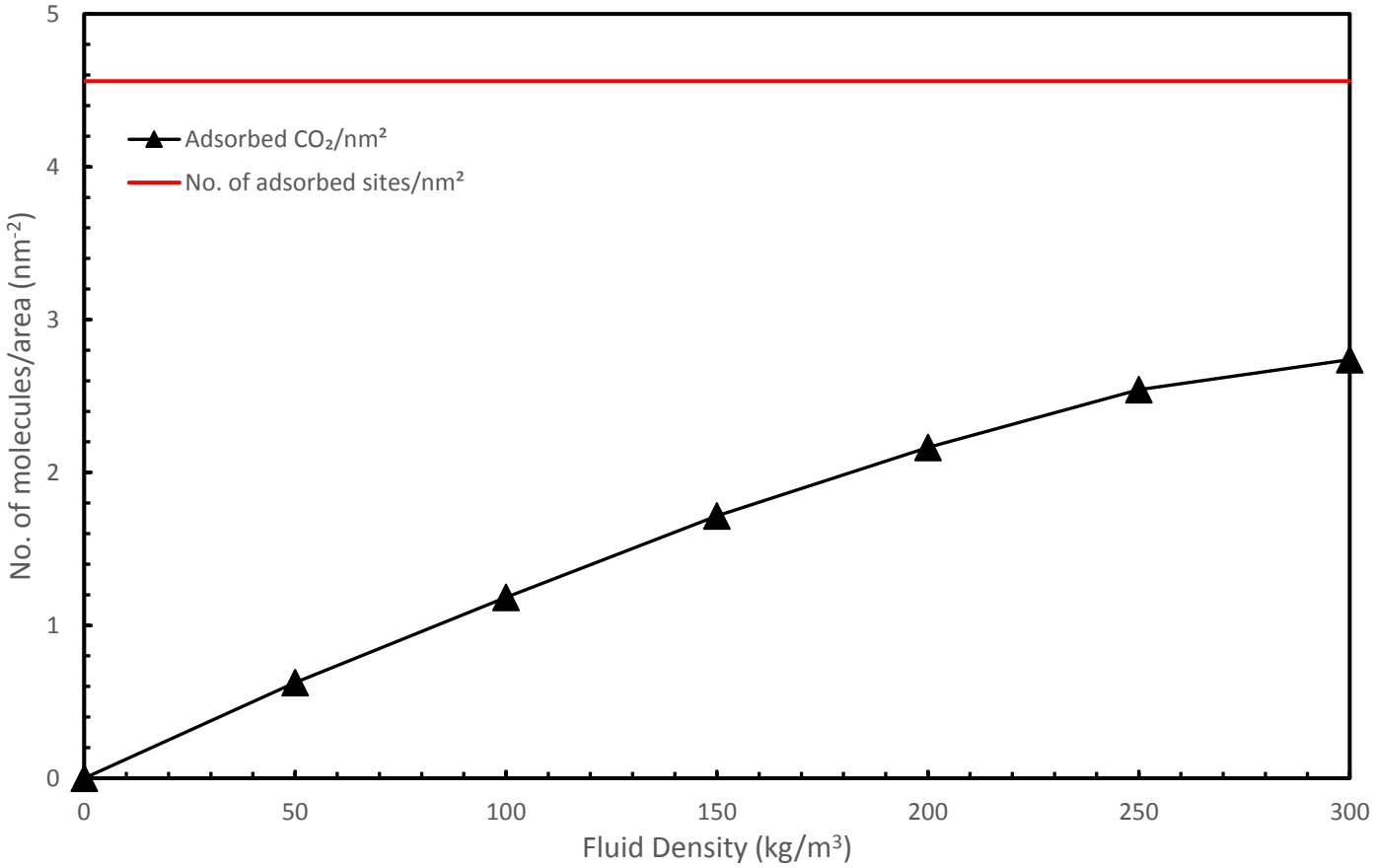

Figure 9: Local Equilibrium Profile AT 375 (data point larger than error bar)

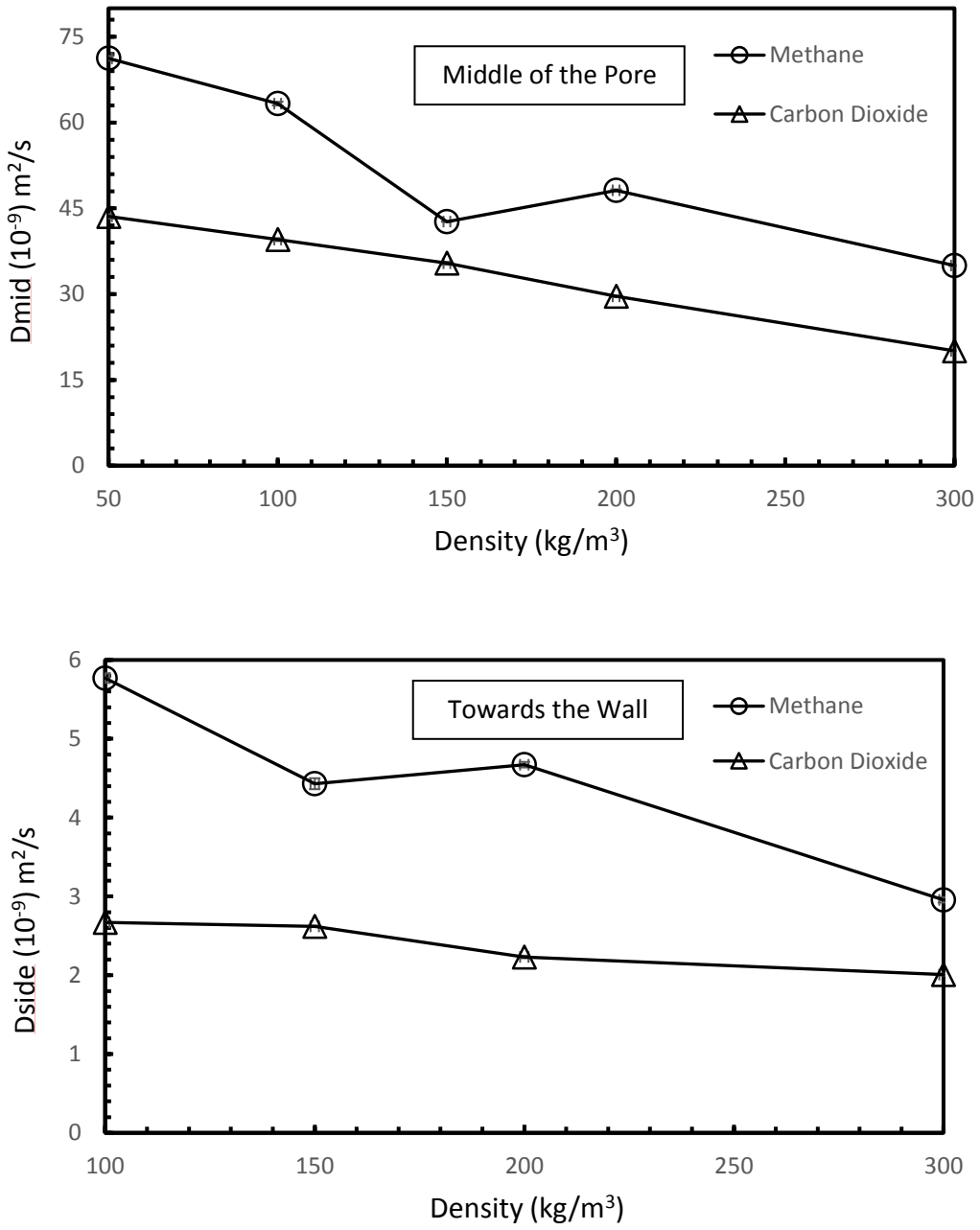

Figure 10: Perpendicular Self-Diffusion Coefficients at Different Mixture densities: Top) middle of the pore, Bottom) towards the wall (data point larger than error bar)

4.4 Effect of Concentration

The effect of changing mixture composition was measured by simulating 3 different systems of methane and carbon dioxide mixtures of density 300 kg/m^3 in a 4 nm silica slit pore. The mole fraction of methane in the three simulated systems was 0.33 , 0.5, and 0.67 respectively. The remaining balance was only carbon dioxide. The temperature in all these systems was kept constant at 375 K.

Figure 11 shows the effect of varying molar composition on the density profiles of the three systems. As expected, in all cases the methane is pushed towards the center of the pore while carbon dioxide, due to polar interactions, shows an affinity to the walls of the pore. It can be deduced that changing the molar ratio does not alter the preferred component for adsorption on the wall. These results qualitatively agree with the results published by Striolo *et al.*[19] who simulated systems of butane and carbon dioxide mixtures in a silica slit pore. The systems examined three different mole fractions which were 0.1 methane, 0.5 methane and 0.9 methane. In each of the cases, it was seen that carbon dioxide has greater affinity towards the wall irrespective of the amount of molecules present in the system.

Furthermore, the height of the peaks in the density profiles is affected by the composition of the system. At greater carbon dioxide compositions, more molecules of carbon dioxide are present and hence occupy more active sites on the wall, resulting in a denser layer of CO_2 at the adsorption site and thus higher peaks. The same trend is seen in Figure 11. At 0.33 methane, more CO_2 is present in the system and thus will occupy more active sites, resulting in higher peaks, whereas at 0.67 methane, less CO_2 is present in the system and thus the height of the peaks will be smaller.

The amount of methane in the center of the pore also increases as the composition of the methane in the system increases. However, as the number of molecules of methane increases, the number of molecules of carbon dioxide decreases and thus there are not enough molecules of carbon dioxide in the system to push all methane molecules to the center of pore. Thus, it is seen that as the composition of methane is increasing, the height of the methane peaks.

Figure 12 shows the perpendicular self-diffusion coefficient of methane and carbon dioxide at the center of the pore as well as towards the wall. In the center of the pore, the perpendicular self-diffusion coefficient of the methane decreases as the composition of methane increases. The same trend is seen with respect to carbon dioxide as the composition of carbon dioxide increases within the system. The enhanced hydrocarbon mobility at the center of the pore at 0.33 methane can be attributed to the preferential adsorption of CO_2 towards the wall. Most of the CO_2 is adsorbed onto the wall and CH_4 is pushed towards the center of the pore. As the system has less CH_4 molecules to begin with, the perpendicular self-diffusion coefficient at the center of the pore is relatively high compared to the other cases.

The same trend is shown by Le *et al.*[49] who simulated a mixture of *n*-octane and carbon dioxide in silica. As the mole fraction of CO_2 in the system was increased from 0.44 to 0.61, the self-diffusion coefficient of *n*-octane increased as well from $10 \times 10^{-9} m^2/s$ to $11.5 \times 10^{-9} m^2/s$. The only difference is that the number of molecules of *n*-octane were kept constant. In this work, as the composition of CO_2 is increased, the molecules of methane are decreased to keep the overall density constant throughout the simulation. Less number of hydrocarbons in the system, and thus in the center of the pore, will mean that there is less steric hindrance and molecular collisions further owing to increase in mobility.

The perpendicular self-diffusion coefficient of CO_2 towards the center of the pore increases as the composition of methane increases in the system. This is because the system has less CO_2 molecules. Since CO_2 molecules are larger than methane molecules, having a lesser number of CO_2 molecules again results in lower steric hindrance and molecular collisions, explaining the trend of CO_2 perpendicular self-diffusion coefficient towards the center of the pore.

Towards the wall of the pore, an interesting phenomena is noted. As the composition of CO_2 increases, so does the perpendicular self-diffusion coefficient. This is because at low CO_2 concentrations, carbon dioxide, which is the preferred component for adsorption, will adsorb onto the high energy active sites. As the concentration of CO_2 in the system increases, there are less high energy active sites available and the CO_2 will occupy more low energy active sites. This will statistically result in an increase in the perpendicular self-diffusion coefficient. These results qualitatively agree with those reported by Le *et al.*[19] and Wang *et al.*[29] who reported an increase in the self-diffusion coefficient of the preferred adsorption component as its concentration increases.

Le *et al.* reported that that self-diffusion coefficient value for CO_2 increased from 6.6×10^{-9}m^2/s to 15.1×10^{-9}m^2/s as the mole fraction of CO_2 in the system is increased from 0.10 to 0.90 for a mixture at 430 K in a silica slit pore. Similarly, Wang *et al.* conducted an experimental study for diffusion of various alkanes in microporous BPL activated carbon. In this study, the alkanes were the preferred component for adsorption on the activated carbon. The diffusivity of *n*-decane increased from 5.5×10^{-4} s^{-1} to 1×10^{-3}s^{-1} as concentration was increased from 30 ppm to 300 ppm, the diffusivity of *n*-octane increased from 2×10^{-3} s^{-1} to 2.2×10^{-3}s^{-1} as concentration was increased from 2500 ppm to 5000 ppm and the diffusivity of *n*-hexane increased from 2×10^{-2}s^{-1} to 5×10^{-2}s^{-1} as concentration was increased from 10000 ppm to 100000 ppm.

The perpendicular self-diffusion coefficient on the side of the wall for methane decreases as the composition of methane increases. This is because at lower compositions of methane, greater concentration of CO_2 is present in the system. As CO_2 will preferably adsorb onto the wall as opposed to CH_4, the perpendicular self-diffusion coefficient of CH_4 is greater.

Simulations were also run while keeping the mixture composition constant but changing the total number of molecules and thus increasing the concentration of the components in the system. The pore size, temperature and mixture composition was kept constant at 4 nm, 375 K and 0.5 methane (mole fraction). The density was varied for each system. These mixture densities were 100 kg/m^3, 200 kg/m^3, and 300 kg/m^3.

Keeping the composition fixed and increasing the overall density, and thus the concentration of the components in the system, results in the perpendicular self-diffusion coefficient to decrease at the center of the pore as well as towards the wall, for both components. This is because as the number of molecules in the system increase, so does the amount of steric hindrance and molecular collision, which result in a decrease in diffusivity. The density profiles are shown in Figure 13 and the perpendicular self-diffusion coefficients are shown in Figure 14. The results qualitatively agree with those published by Le *et al.*[19] who showed a decrease in self-diffusion coefficient for both butane and carbon dioxide in an equimolar mixture as the total number of molecules in the system were increased. As the total number of molecules in the system increased from 100 to 500, the self-diffusion coefficient for both methane and carbon dioxide decreased from 15.8×10^{-9}m^2/s to 5.2×10^{-9}m^2/s and 3.7×10^{-9}m^2/s to 2.5×10^{-9}m^2/s respectively.

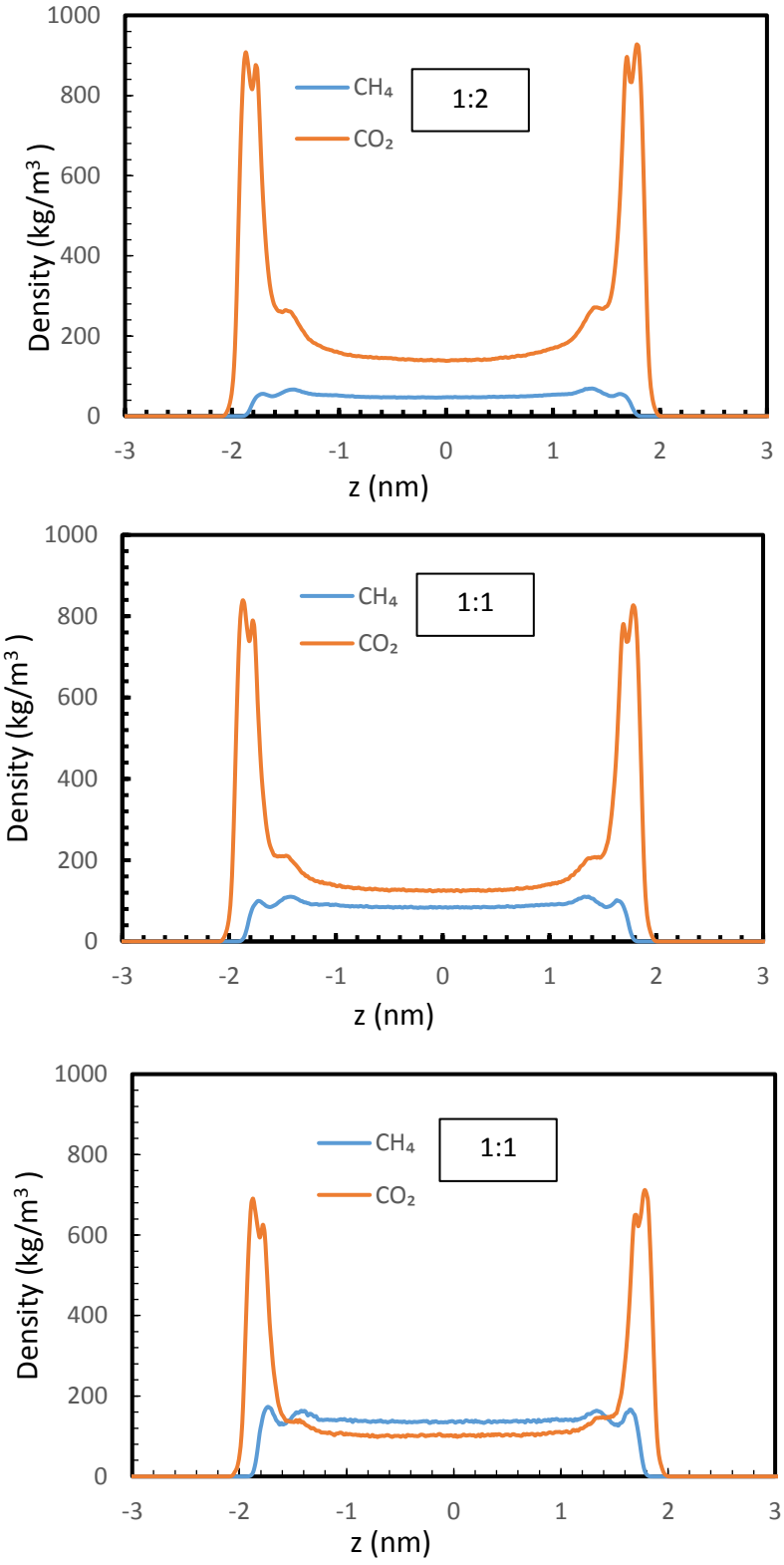

Figure 11: Density Profiles for Methane and Carbon Dioxide at Different Mixture Compositions: Top) 1:2, Middle) 1:1 and Bottom) 2:1

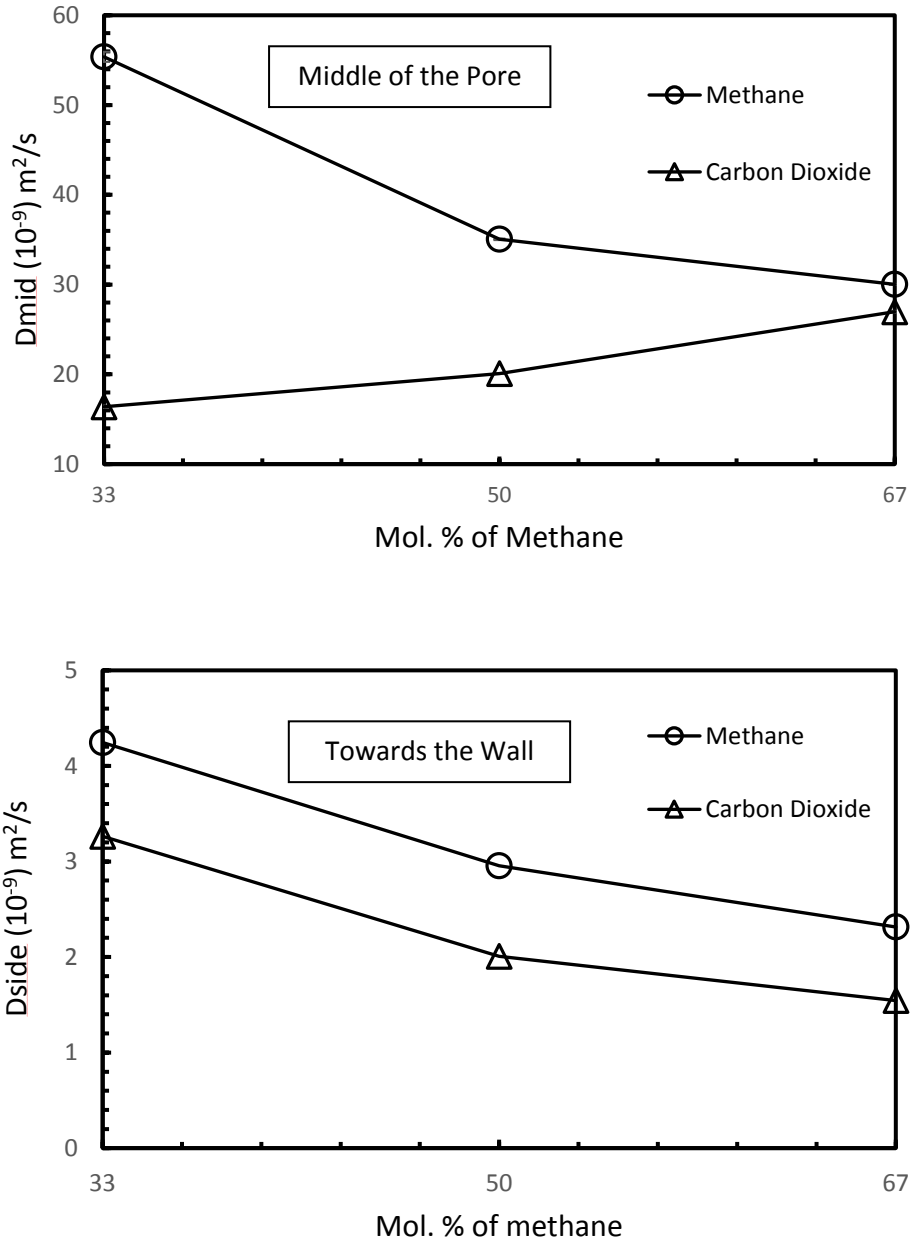

Figure 12: Perpendicular Self-Diffusion Coefficients at Different Mol. % of Methane: Top) middle of the pore, Bottom) towards the wall (data point larger than error bar)

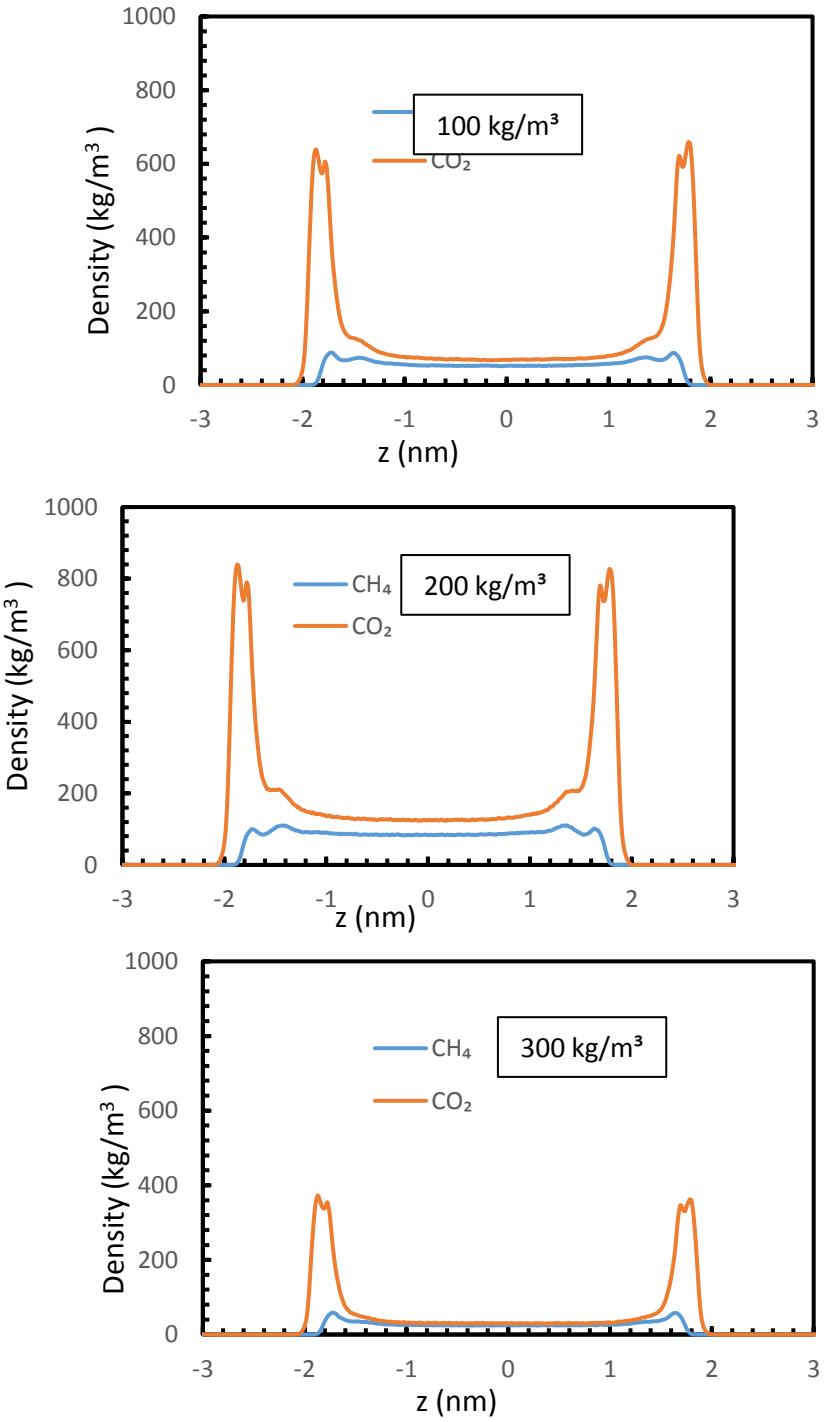

Figure 13: Density Profiles for equimolar mixture of Methane and Carbon Dioxide at Different Densities: Top) 100 kg/m^3, Middle) 200 kg/m^3 and Bottom) 300 kg/m^3

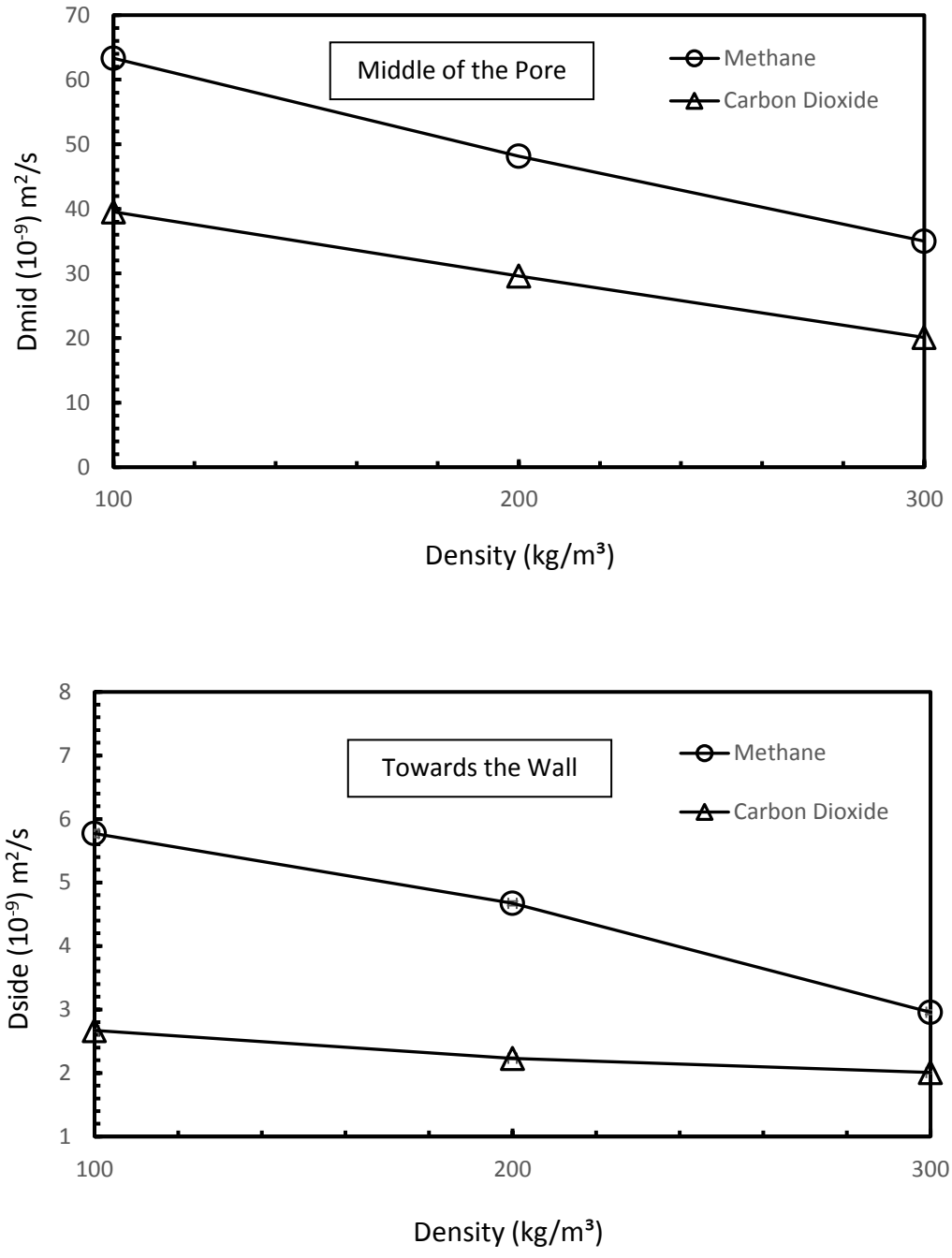

Figure 14: Perpendicular Self-Diffusion Coefficients at Different Densities: Top) middle of the pore, Bottom) towards the wall (data point larger than error bar)

4.5 Effect of System Temperature

Three systems, containing a 1:1 molar ratio mixture of CO_2 and methane at a total mixture density of 300 kg/m^3 within a 4 nm pore of silica at three different temperatures, were investigated. The temperatures of these systems were 300 K, 375 K and 450 K respectively. The density profiles and self-diffusion coefficient of the fluid components in these systems was calculated to understand the effect of changing the temperature. Figure 15 shows the density profile of CO_2 and methane in each of these systems and Figure 16 shows the self-diffusion coefficients in the perpendicular direction for the same components.

Firstly, looking at the density profiles for methane, it can be noticed that as the temperature of the system increases from 300 K to 450 K, the amount of methane in the center of the pore increases, whereas the amount of methane being adsorbed onto the walls decreases. A similar trend is seen when analyzing the density profiles of CO_2. Consistent with the previously shown figures, the peaks of CO_2 are closer to the wall compared to the peaks of methane. For all temperatures, it can be deduced from the plots that the positioning of the peak is not affected by change in temperature. As the temperature is increased, more CO_2 is found towards the center of the pore. At a temperature of 300 K, most of the CO_2 is adsorbed onto the wall and the density of CO_2 at the center is very low. This indicates the preferential adsorption of CO_2 over methane on the wall. As the temperature increases, CO_2 is still the preferred component with respect to adsorption onto the wall. However, the amount of CO_2 and methane being adsorbed onto the wall reduces with increasing temperature. The decreased amount of CO_2 as well as methane at higher temperatures can be attributed to the increase in thermal motion of the particles[19]. As the temperature increases,

the kinetic energy of the particles increases as well. Hence, a greater amount of the particles within the system have enough energy to break away from the adsorption on to the silica surface. Another important feature to note with respect to the positioning of the CO_2 molecules near the wall, is the formation of a multilayer as represented by the multiple peaks. As the temperature is increased to 450 K, the multilayer of CO_2 disappears to form a single peak.

Similar results have been published in literature. Le *et al.*[19] simulated systems of butane and carbon dioxide of varying molar composition at three different temperatures: 290 K, 343 K and 430 K. Irrespective of the composition of the fluid within the system, the same trend was seen in all cases with increase in temperature, which has been validated in this work as well. The number density of CO_2 at 290 K for an equimolar mixture was approximately 7 molecules/nm^3 (at the wall). As the temperature was increased to 343 K and then 430 K, this number density decreased to approximately 4 molecules/nm^3 and 2.75 molecules/nm^3 respectively. The increase in thermal motion due to greater kinetic energy allows the molecules to escape the active sites on the wall. For methane, the same trend was observed and it is validated by this work. The number density of methane decreased from approximately 3.8 molecules/nm^3 to 3 molecules/nm^3 . The decrease in the density of methane at the wall is not as pronounced as it is for the case of CO_2. This is attributed to the fact that CO_2 is the component that occupies most active sites due to preferential adsorption.

Santos *et al.*[26] simulated a system consisting of CO_2 and methane in a calcite nanopore at three different temperatures: 325 K, 375 K, 425 K. The results shown qualitatively matched that shown in other literature data as well as the results shown in this work. The results showed that at high densities and low temperatures, the concentration of CO_2 is much higher than that at higher temperatures. Furthermore, at all temperatures, CO_2 concentration at the wall is greater than the

concentration of methane, validating the preferential adsorption of CO_2 shown in this work. This is due to CO_2 having favorable polar interactions with calcite as opposed to methane with calcite. CO_2 will show similar favorable polar interactions with silica as well. The number density of CO_2 towards the wall in the system simulated by Santos *et al.* is approximately 35 molecules/nm^3 at 325 K which decreases to 29 molecules/nm^3 and then 27.5 molecules/nm^3 as temperature is increased to 375 K and 425 K respectively. The number density of CH_4 decreases from approximately 7.5 molecules/nm^3 to 5.5 molecules/nm^3 as temperature is increased from 325 K to 425 K respectively.

Khosrokhaver *et al.*[52] used the manometer method to measure the excess sorption isotherms for CH_4 at 308 K, 318 K and 336 K at pressures up to 105 bar on black shale. The experiment showed that as the temperature increased, the excess sorption of the methane decreased. For example, at 80 bar, the excess sorption for methane was approximately 0.03 mmol/g at 308 K which decreased to below 0.02 mmol/g at 318 K and reached 0 mmol/g at 336 K. Gasparik *et al.*[53] conducted an experiment to measure the excess sorption of methane on organic-rich shale at 25 MPa and varying temperatures: 318 K, 338 K and 348 K. The results showed that excess sorption decreased as the temperature increased.

The perpendicular self-diffusion coefficient at the center of the pore increases with increasing temperature for both CO_2 and methane. This is in qualitative agreement with the results presented by Le *et al.*[19] who simulated system of butane and CO_2 mixtures with in a silica nanopore at different temperatures. The results reported showed that for all molar compositions, as the temperature increased, so did the self-diffusion of both components in the system. As the temperature increases, the kinetic energy of the molecules increases which increases the mobility

of the molecules. A similar trend is seen with the perpendicular self-diffusion coefficients for both components towards the wall of the pore. Due to having higher kinetic energy, the molecules are able to overcome the energy required to break free from their adsorption. In all cases, the self-diffusion coefficient of methane is greater than that of CO_2 due to the reasons explained before. The difference in magnitude of perpendicular self-diffusion coefficient remains similar to results shown in previous chapters and one can deduce that the effect of temperature is more pronounced in the center of the pore.

Figure 17 shows an Arrhenius plot of the perpendicular self-diffusion coefficient of carbon dioxide and methane towards the pore of the wall. From the linear fit of the data points, it is possible to calculate the activation energy of diffusion associated each component in the fluid. The slope of the linear fit is the ratio of activation energy to the universal gas constant. As such, the activation energy of methane and carbon dioxide is calculated as 3.58 kJ/mol and 5.65 kJ/mol respectively. From these values, it can be deduced that near the wall of the pore, CO_2 indeed requires a greater activation energy to diffuse when compared to CH_4. This confirms that CO_2 adsorbs preferentially at the active sites and thus has a lesser mobility compared to CH_4.

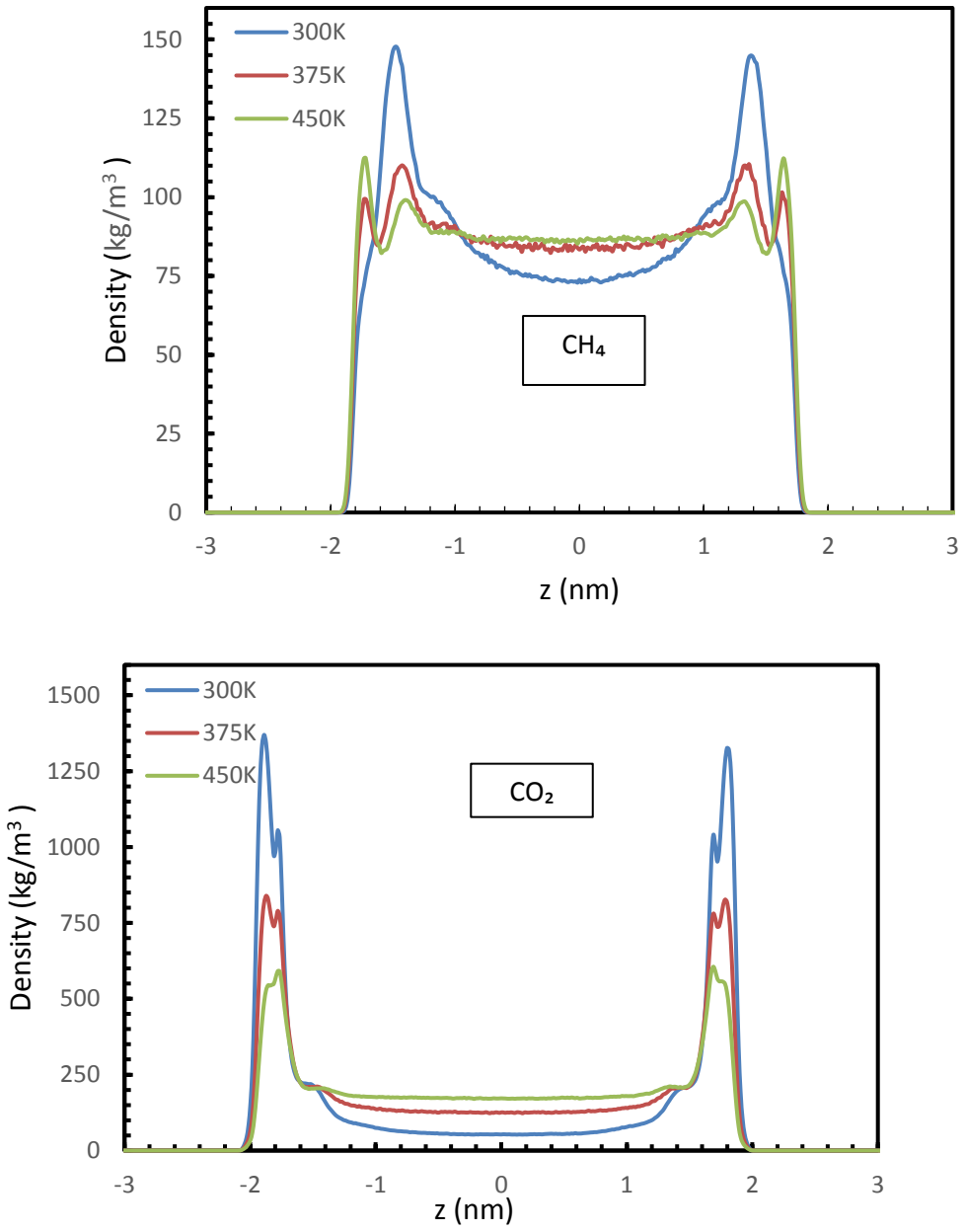

Figure 15: Density Profiles Different Temperatures: Top) Methane, and Bottom) Carbon Dioxide

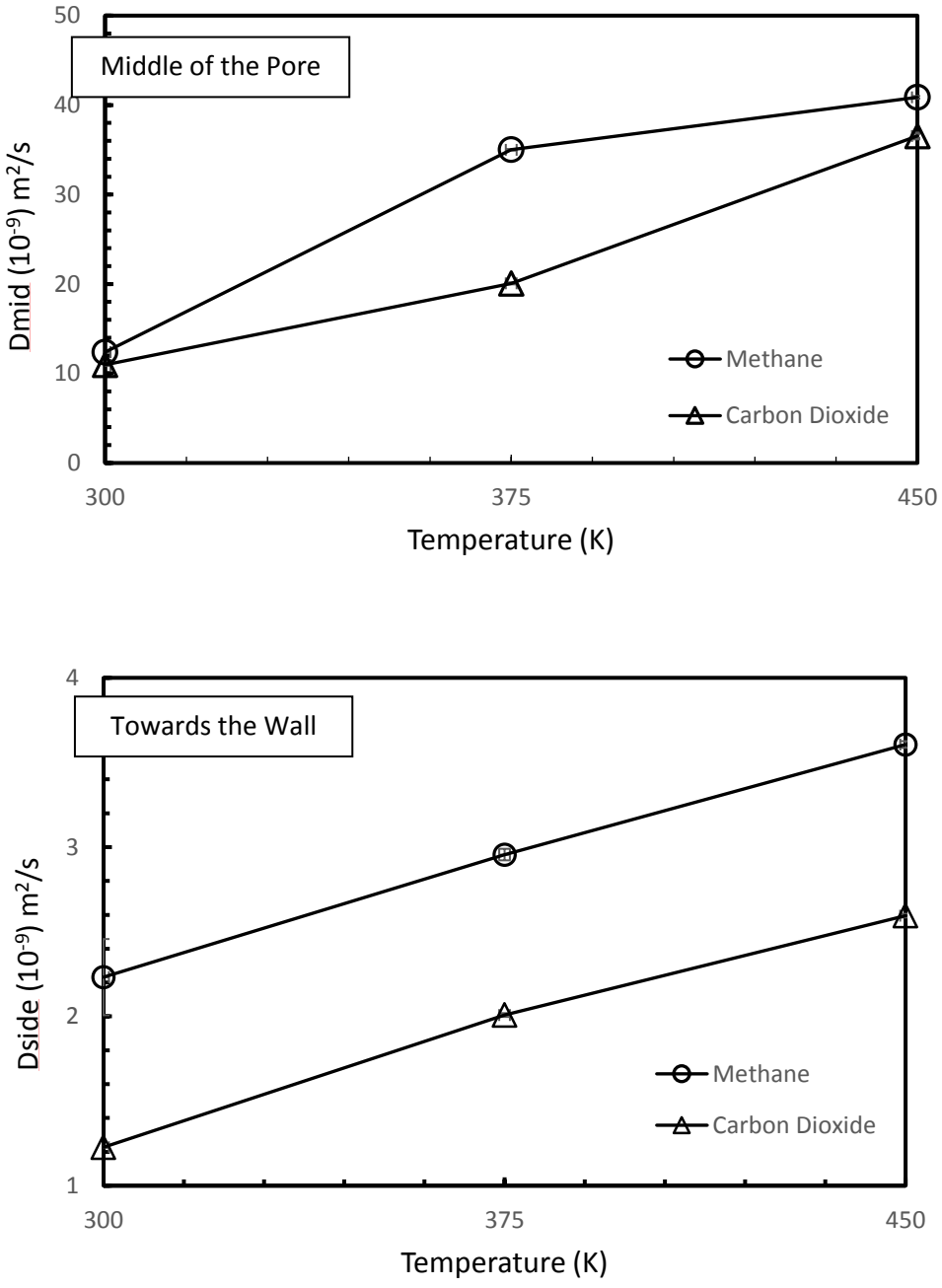

Figure 16: Perpendicular Self-Diffusion Coefficients at Different Temperatures: Top) middle of the pore, Bottom) towards the wall (data point larger than error bar)

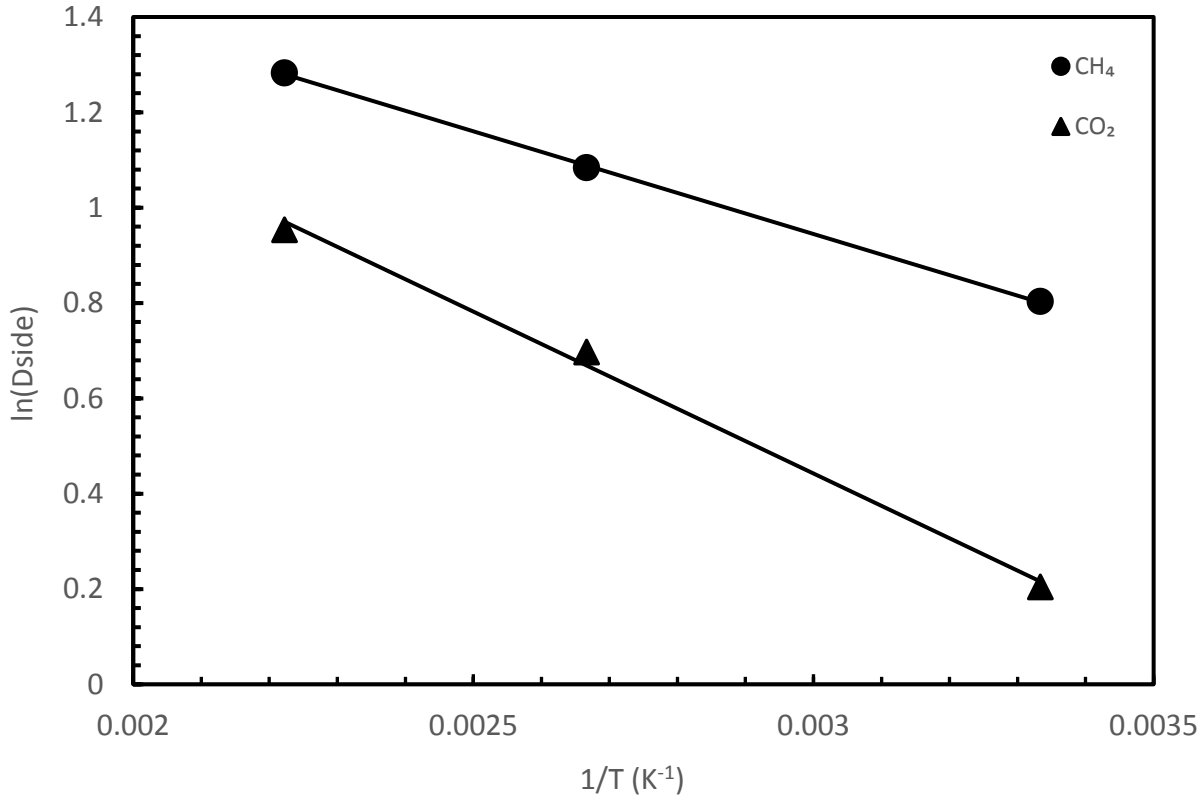

Figure 17: Arrhenius Plot for the Self-Diffusion Coefficient of Methane and Carbon Dioxide towards the Pore of the Wall (data point larger than error bar)

4.6 Effect of Pore Size

The effect of pore size was studied by simulating three different systems consisting of an equimolar mixture of carbon dioxide and methane of density 300 kg/m^3 and temperature of 375 K, in a silica slit pore of three different sizes: 3 nm, 4nm and 8 nm. The perpendicular self-diffusion coefficients at the center of the pore and towards the wall are shown in Figures 18 and 19 respectively.

One can see from Figure 18 that increasing the pore size does not cause any changes in the preferred adsorption component within the fluid. In all three cases, the preferred component is carbon dioxide and the less preferred component is methane owing to the polar interactions between CO_2 and silica. The peaks are the highest for the system where the pore size is 8 nm and they decrease as the pore size decreases. The reason for this is that there are more molecules in the system as the pore size increases to keep the density constant. The active sites remain the same for since there are more molecules present in the system to adsorb on to the wall. Since, active sites do not change, constantly increasing the pore size and hence the number of molecules in the system will only increase the size of the peaks till all the active sites have been occupied. Thus, one can see that as the pore size increases, the height of the peaks increases but at a decreasing rate. For the system with a 3nm pore, one can see from the graph that the height of the peak is represented by the 755 kg/m^3 density mark. As the pore size is increased to 4 nm, the density mark representing the peak increases to 830 kg/m^3. Further increasing the pore size to 8 nm, increases the density mark representing the peak to 990 kg/m^3.

At the center of the pore, the density remains relatively the same for methane, slightly decreasing as the pore size increases. On the other hand, the density of CO_2 at the center of the

pore increases as the pore size increases. Since the number of active sites are constant, more CO_2 is statistically found at the center of the pore as pore size increases. However, since methane is not preferably adsorbed, the greatest number of molecules for it remain in the center of the pore and increase linearly as the pore size increases. Hence, the density of methane at the center remains relatively same.

The results shown in this work have been qualitatively validated with that shown in literature, e.g. Santos *et al.*[36] reported results for a system consisting of CO_2 and methane in a calcite nanopore, at 375 K for three different pore sizes: 3 nm, 5.5 nm, and 8 nm. The number density of CO_2 in the adsorption layer increases from 22 molecules/nm^3 to 27 molecules/nm^3 as pore size increases from 3 nm to 5.5 nm. As the pore size is increased from 5.5 to 8 nm, the number density in the adsorption layer does not change. This indicates that the number of active sites on the calcite wall have been occupied. The same trend was seen in this work where although not all active sites of the silica were occupied, the increment in height of the peak was reducing as the pore size increased.

Rother *et al.*[54] conducted an experimental study to understand the effect of pore size on excess sorption of supercritical CO_2 in mesoporous CPG-10 silica glass. The results showed that CO_2 storage capacity is enhanced at low temperatures and narrow pore sizes. In fact, for a density of 300 kg/m^3 the excess sorption of supercritical CO_2 was recorded as approximately 15 μmol/m^2 in the adsorption layer in a pore size of 7.5 nm whereas it was recorded as approximately 39 μmol/m^2 in the adsorption layer in a pore size of 35 nm.

The perpendicular self-diffusion coefficient for both components at the center of the pore as well as towards the wall, increase with increasing pore size. As the pore size is increased, the

effect of the wall potential decreases and the fluid in the middle of the pore behaves more as a bulk fluid. This is why at the center of the pore, once can see the perpendicular self-diffusion coefficients for both components increasing and most likely reaching their self-diffusion values in bulk. This same trend has been validated by Franco *et al.*[51] who simulated methane within a calcite nanopore. The results published showed that as the pore size increased, so did the perpendicular self-diffusion coefficient at the center of the pore, approaching the self-diffusion of methane in bulk for the specified conditions. At a pore size of 1.75 nm, the perpendicular self-diffusion coefficient of methane was reported to be approximately $32 \times 10^{-9} \mathrm{m}^2/\mathrm{s}$. The perpendicular self-diffusion coefficient increased to approximately $95 \times 10^{-9} \mathrm{m}^2/\mathrm{s}$ at a pore size of 7 nm. At 14 nm, the perpendicular self-diffusion coefficient further increased to $112 \times 10^{-9} \mathrm{m}^2/\mathrm{s}$, approaching the self-diffusion coefficient in the bulk, which was approximately $125 \times 10^{-9} \mathrm{m}^2/\mathrm{s}$ in the specified conditions. Zhou and Wang[54] reported similar results for CO_2 in carbon slit pores that qualitatively agree with the results from this work.

Towards the wall of the pore, one can see the perpendicular self-diffusion coefficient also increasing as the pore size increases for both components. In the case of CO_2, this may be attributed to the fact that as more CO_2 is present to occupy the same number of active sites, with increasing pore size, CO_2 occupies more low energy active sites resulting in the perpendicular self-diffusion coefficient to increase as the pore size is increased. The perpendicular self-diffusion coefficient of methane increases with increasing pore size, possibly due to the fact that as more CO_2 is in the system, it will adsorb on to more active sites. The CH_4 will have less opportunities to adsorb on to the wall resulting in the perpendicular self-diffusion coefficient to increase.

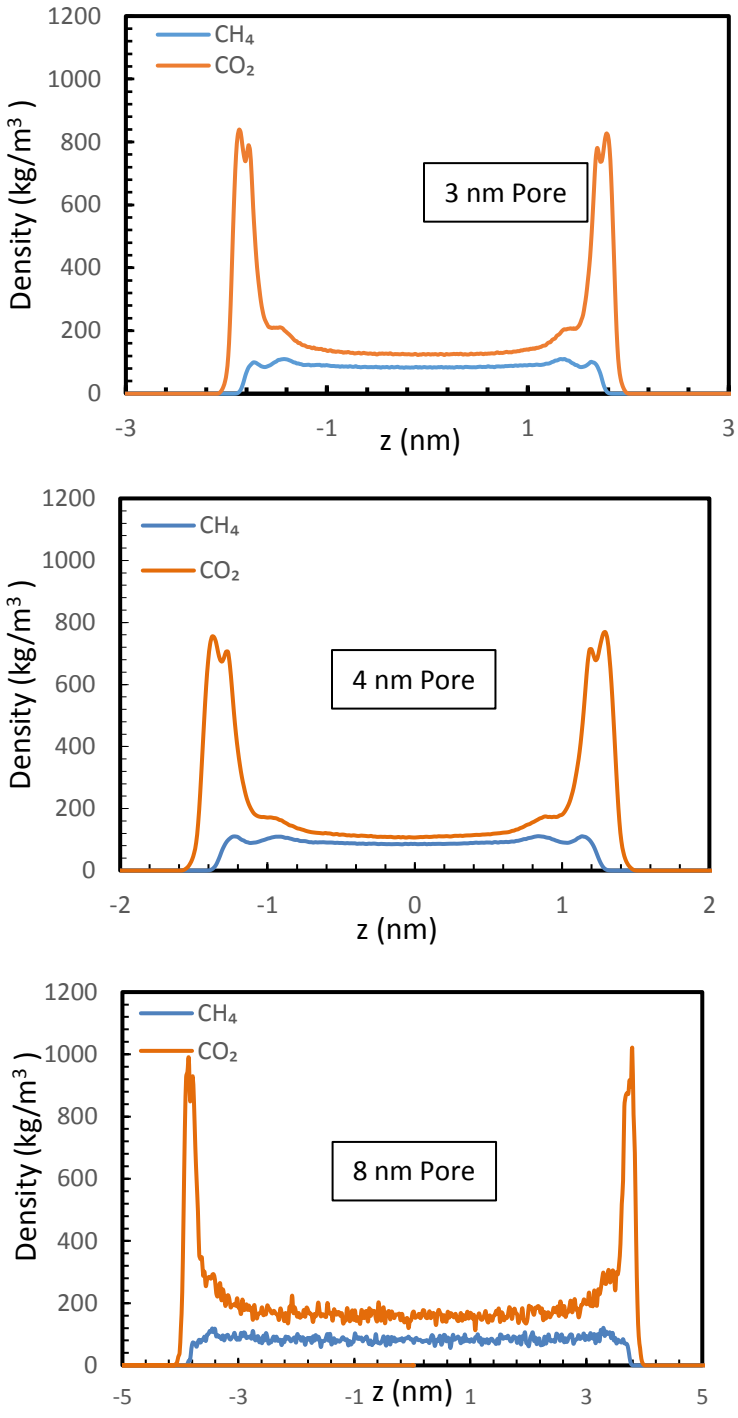

Figure 18: Density Profiles: Top) 3 nm pore, middle) 4 nm pore, and Bottom) 8 nm pore

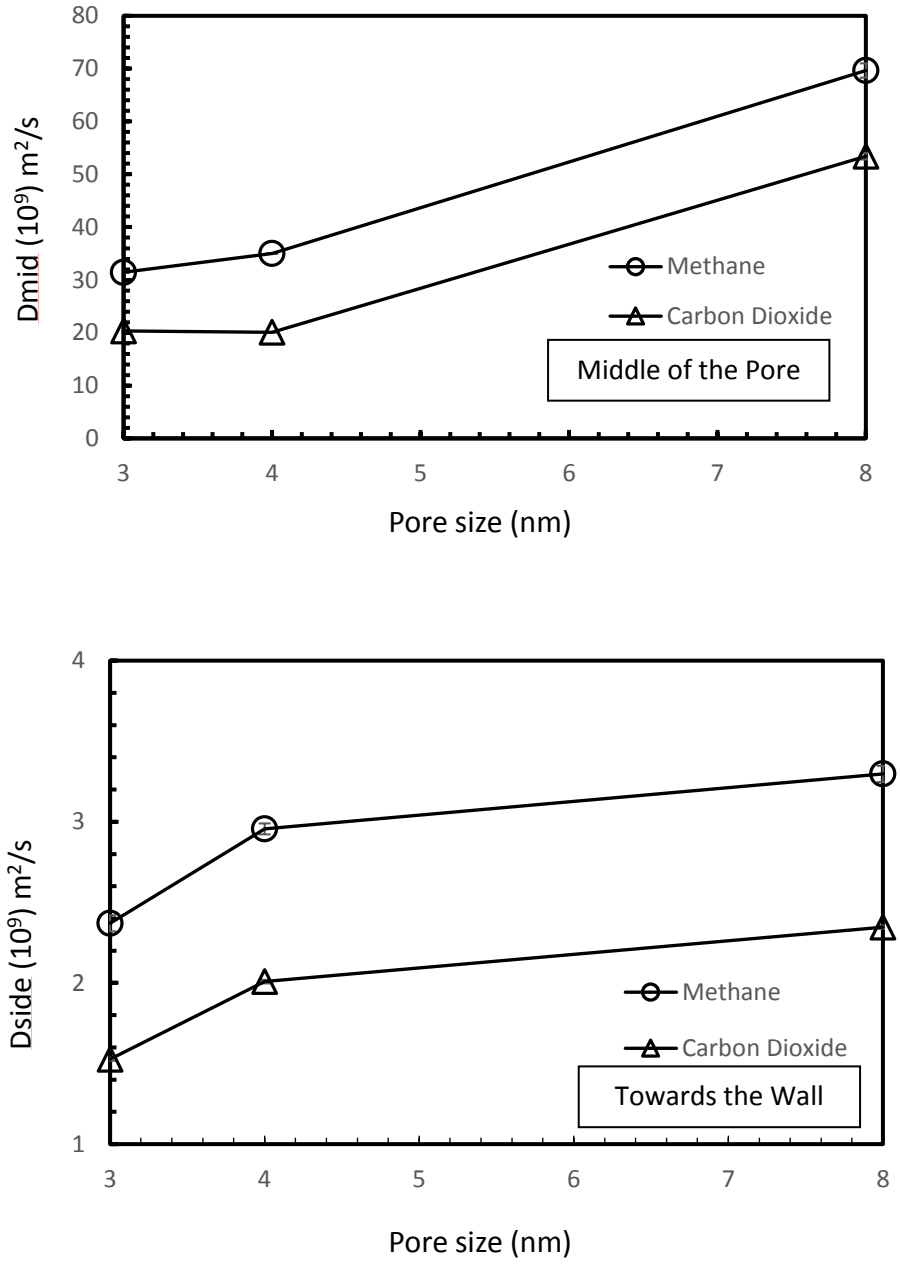

Figure 19: Perpendicular Self-Diffusion Coefficients at Different Pore sizes: Top) middle of the pore, Bottom) towards the wall (data point larger than error bar)

4.7 Effect of Pore Material

The effect of pore material was studied by simulating 5 different systems containing methane at a density of 350 kg/m^3 and temperature of 300 K, within a pore size of 10 nm. The material of the pore was varied in each simulation. The materials used were silica, muscovite, magnesium oxide, alumina, and calcite. The force fields used for methane was TraPPE[32], and that for all substrates except for calcite, was ClayFF[22]. For calcite, the force field use was one present by Xiao *et al.*[37].

Figures 20-24 show the density profiles of methane in each slit pore made out of different materials. The forcefield parameters can be found in chapter III, section 3.3. The curves exhibit symmetry with respect to the center of the pore. The most prominent feature of the curves are the two distinct peaks at each end of the graph. These ends represent the walls of the slit-shapes nano pores. The general understanding that can be obtained from these results is that due to the potential of the wall, an area of heterogeneity is created within the fluid. Naturally, the effect of the wall potential are greater closer to the wall and not significant towards the center of the pore since the pore size is quite large (10 nm). Thus, at the center of the pore, one can see the fluid acting homogenously as it would in bulk conditions, and closer to the wall it can be seen that the fluid is being attracted and thus closely adsorbing onto the wall resulting in two distinct peaks and areas of high fluid density. Further comparing the graphs within themselves, it is noticed that the strongest wall potential onto the fluid is exhibited by Calcite and the weakest, by silica.

Bui *et al.*[27] simulated methane in the same pores but saturated with water. The results of the work showed that self-diffusion coefficient of methane is highest in silica at 8.00×10^{-10}m^2/s

followed by magnesium oxide ($5.50 \times 10^{-10} m^2/s$), alumina ($3.25 \times 10^{-10} m^2/s$), muscovite ($1.90 \times 10^{-10} m^2/s$), and finally calcite ($1.80 \times 10^{-10} m^2/s$). Higher self-diffusion would mean greater mobility and thus the molecules of methane are not adsorbed on to the substrate wall as strongly compared to when the self-diffusion coefficient is low. By this logic, one would expect that the density profiles of methane will have the highest peak within calcite followed by muscovite, alumina, magnesium oxide and finally silica. However, the order identifies with respect to highest to lowest methane peak - in this work it is calcite > alumina > magnesium oxide > muscovite > silica. Based on this work, methane in muscovite would be expected to have a self-diffusion coefficient between that of methane within silica and magnesium oxide. One possible reason for this discrepancy is that in the work published by Bui *et al.* the pores are saturated with water. The water molecules may not be occupying as many saturation sites as they would with silica, alumina, or magnesium oxide. This might be a possible reason for the discrepancy in the results.

Furthermore, Figures 20-24 also show the heat maps that were plotted to showcase the adsorption of the methane onto the different substrates. The results of the heat maps of the surface of the wall showed to be in alignment with what was see from the density profiles. It can be seen that the heat maps are similar for silica and muscovite as their density profiles are similar. As one moves from magnesium oxide to alumina to calcite, one notices that the heat maps gets busier and there is an increasing emergence of high-density pockets.

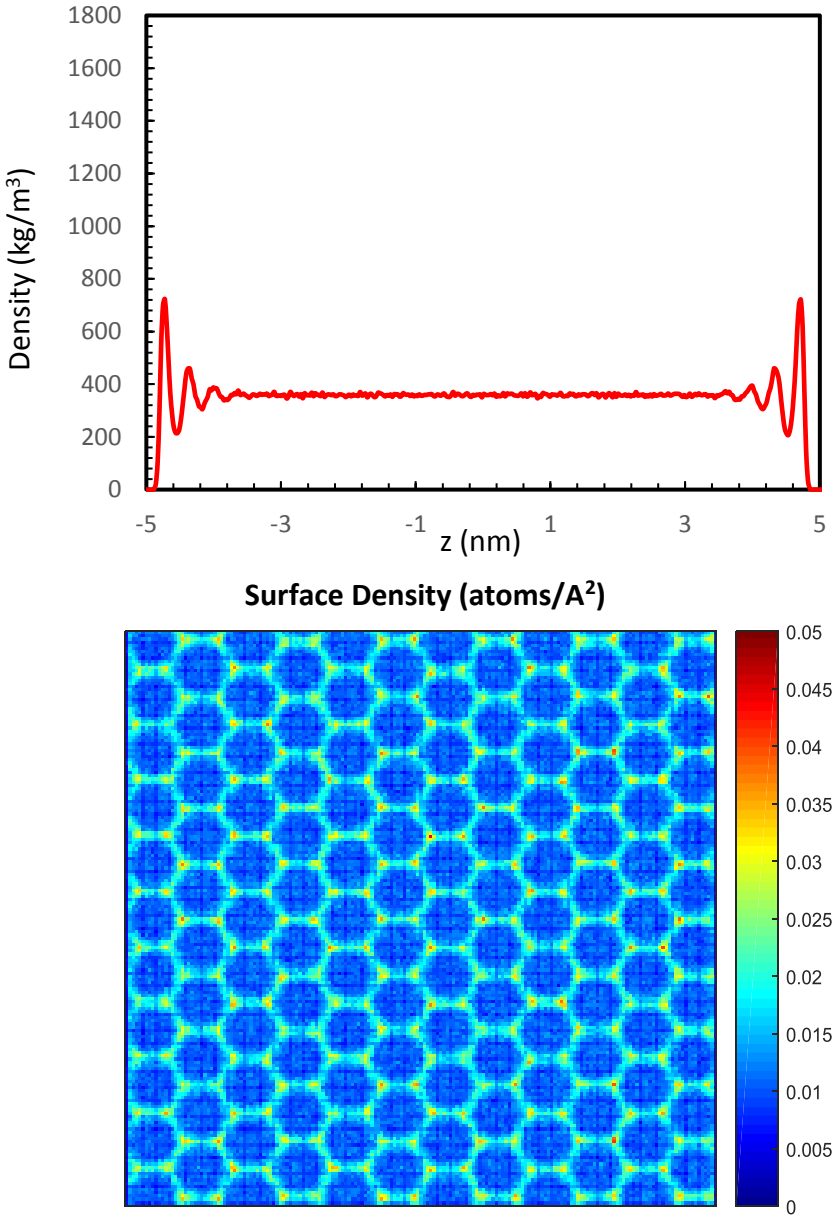

Figure 20: Top) Density Profile of Methane in 10 nm Silica Slit Pore, and Bottom) Heat map near the pore wall (heat maps provided by Dr. Maria Apostolopoulou, University College London)

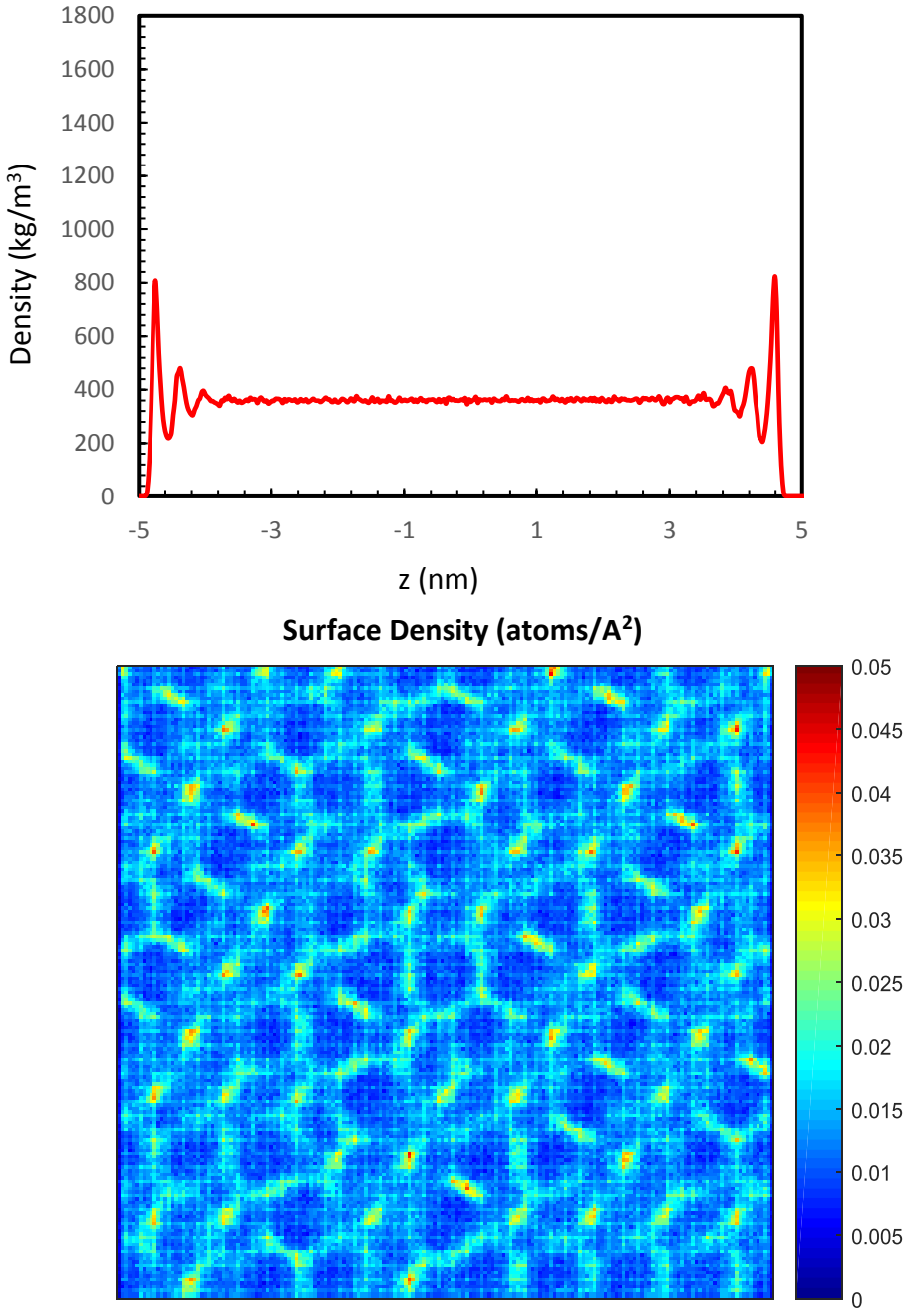

Figure 21: Top) Density Profile of Methane in 10 nm Muscovite Slit Pore, and Bottom) Heat map near the pore wall (heat maps provided by Dr. Maria Apostolopoulou, University College London)

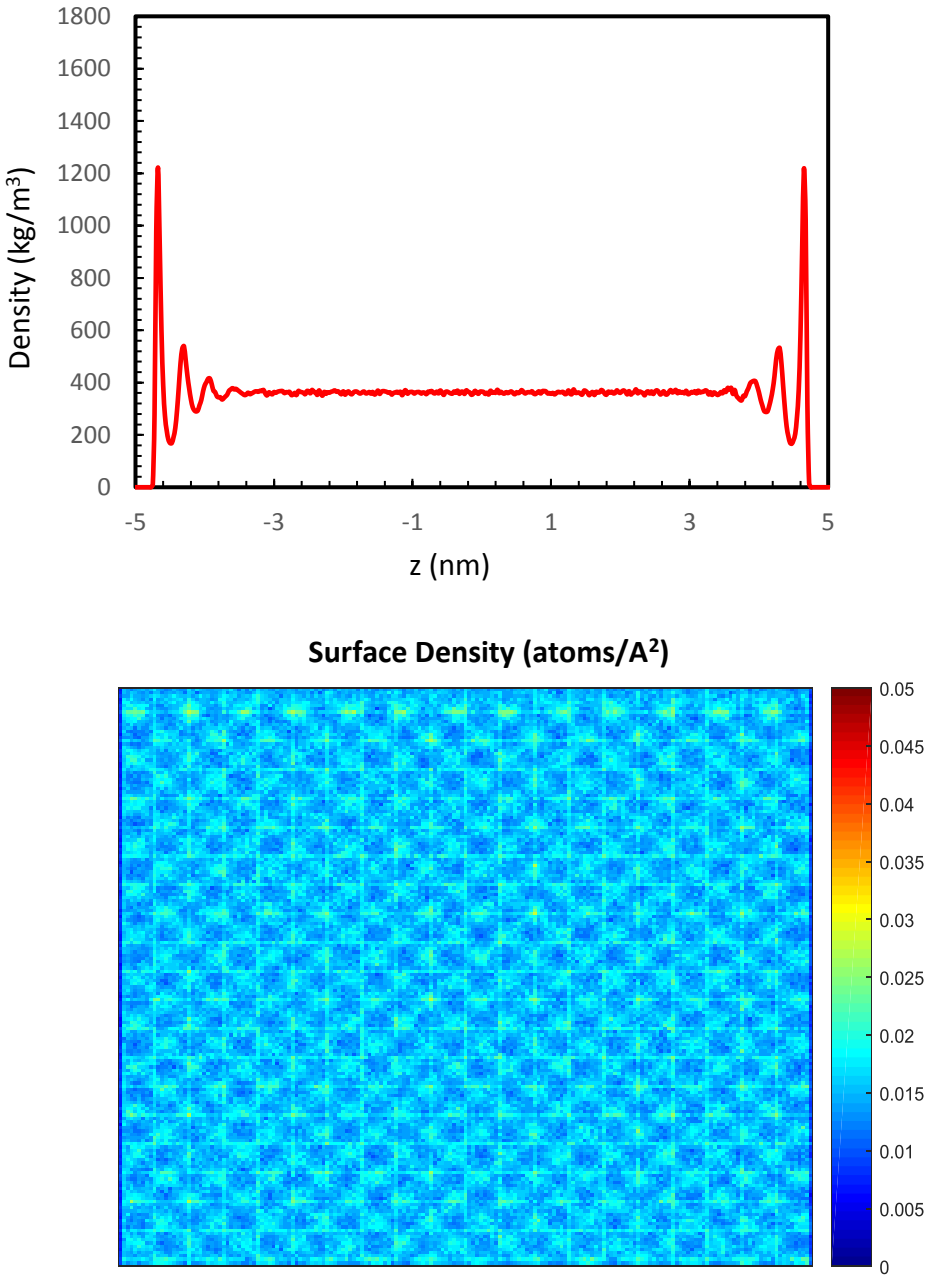

Figure 22: Top) Density Profile of Methane in 10 nm Magnesium Oxide Slit Pore, and Bottom) Heat map near the pore wall (heat maps provided by Dr. Maria Apostolopoulou, University College London)

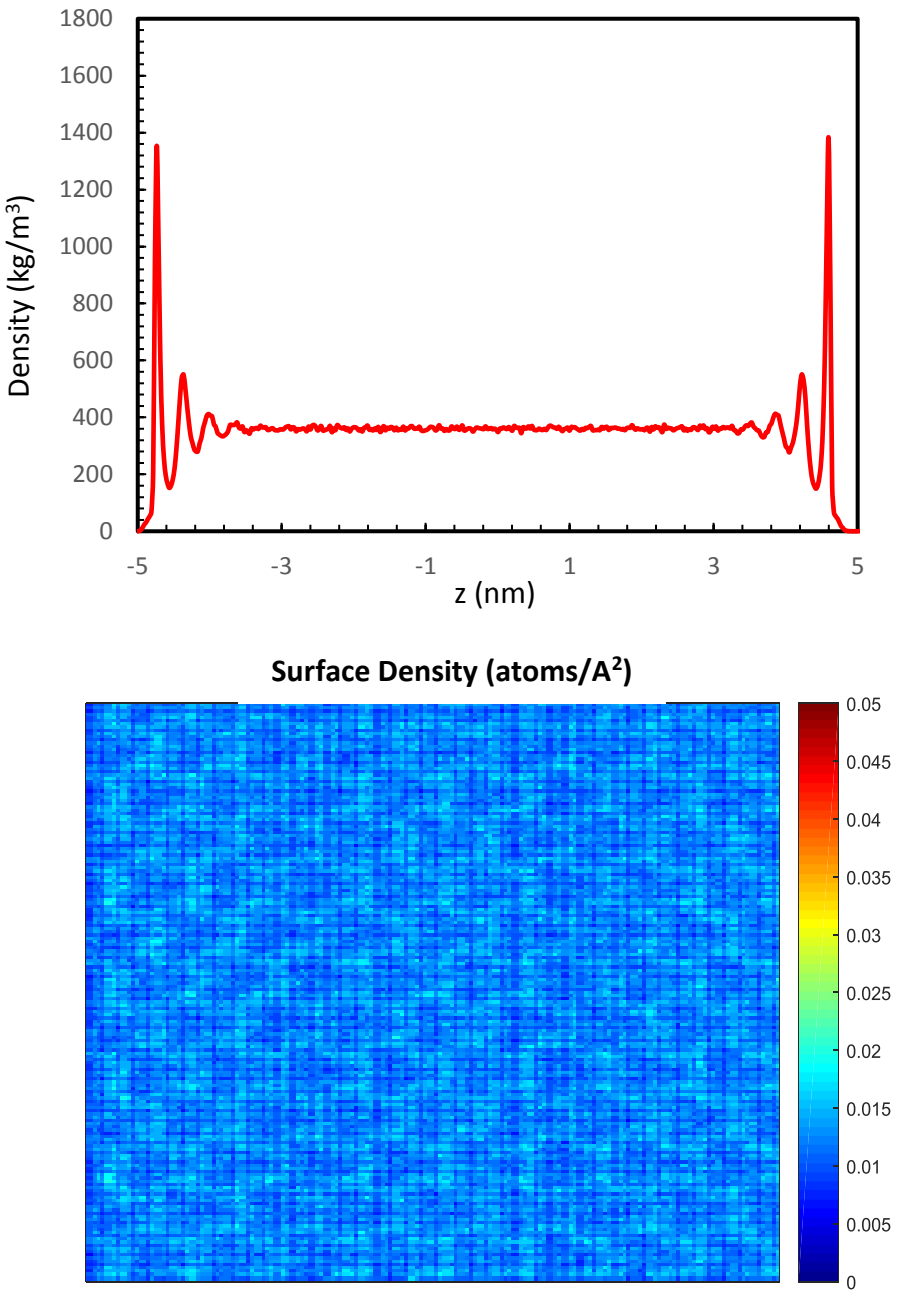

Figure 23: Top) Density Profile of Methane in 10 nm Alumina Slit Pore, and Bottom) Heat map near the pore wall (heat maps provided by Dr. Maria Apostolopoulou, University College London)

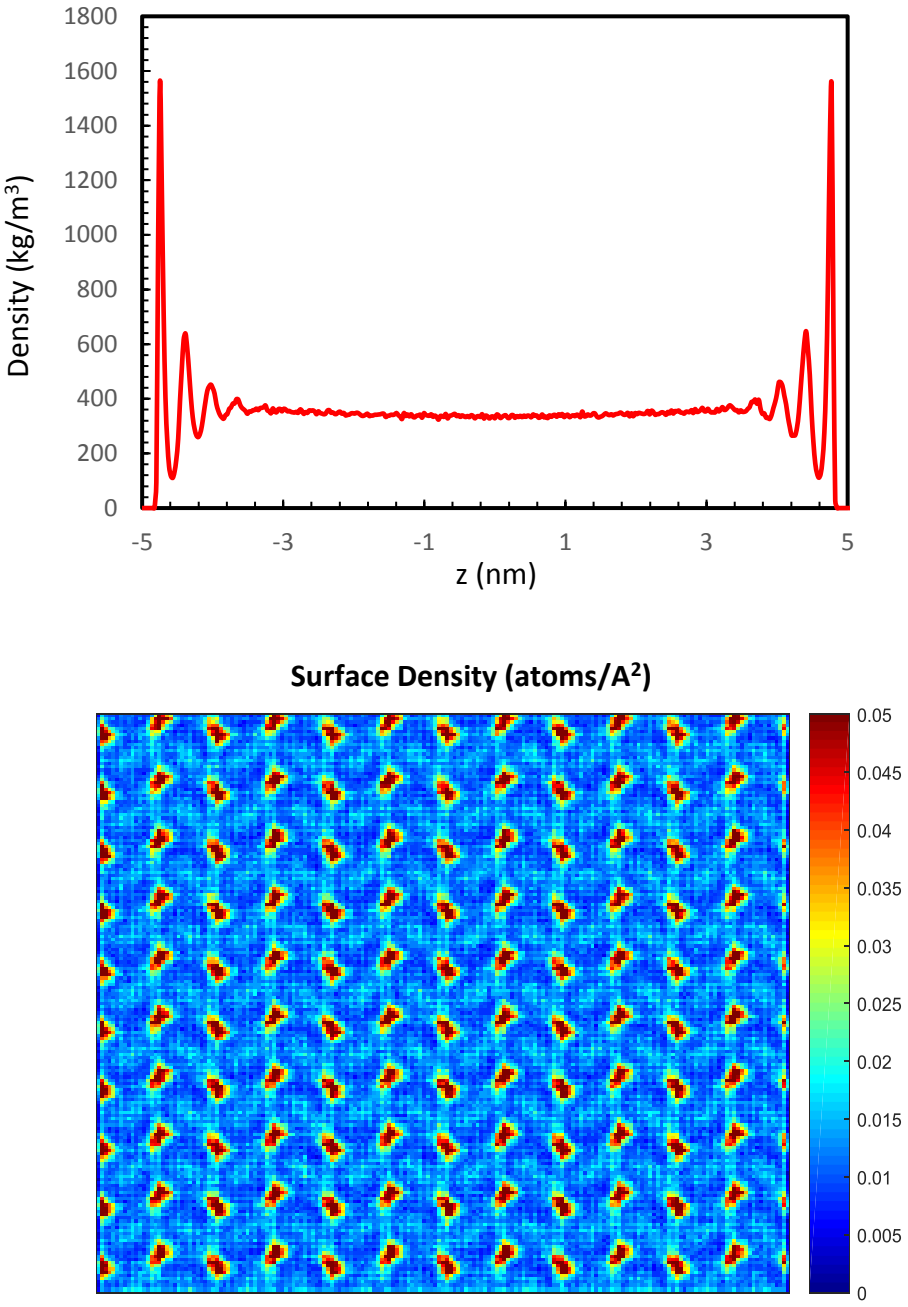

Figure 24: Top) Density Profile of Methane in 10 nm Calcite Slit Pore, and Bottom) Heat map near the pore wall (heat maps provided by Dr. Maria Apostolopoulou, University College London)

4.8 Effect of Moisture

The effect of moisture was studied by simulating three different systems. The first system was an equimolar mixture of CH_4 and CO_2 along with 3% molar water in a 4 nm silica pore. The second system was a mixture of *n*-octane and CO_2 at a molar ratio of 1:2 along with 3% molar water in a 4 nm silica pore. The third system was *n*-decane and CO_2 at a molar ratio of 1:2 along with 3% molar water in a 4 nm silica pore. In all cases, the temperature was kept constant at 375 K. The first system had a simulation time of 30 nanoseconds whereas the other systems had a simulation time of 60 nanoseconds since systems with longer chain hydrocarbons are expected to take longer to reach equilibrium.

Looking at Figure 25, one can notice all the water in the system has been adsorbed onto the walls of silica. It has been reported by Wang *et al.* via simulations and by Pan *et al.*[64] via experiments that introducing moisture tends to significantly decrease the amount of adsorption of CH_4. This can be seen when comparing Figure 25 to Figure 7. Without moisture, the peak in Figure 7 for a fluid density of 300 kg/$^{-3}$ represents a methane density of 97 kg/m^3. When moisture is present, the peak in Figure 25 for the same fluid density represents a methane density of 55 kg/m^3. This means that including 3% water in the specified system decreased the adsorption capacity from a density perspective by 47%. Wang *et al.* for the studied systems reported a decrease in methane adsorption capacity by 67% in organic pores and 33% in inorganic pores by addition of 0.2 g/cm^3 water.

The perpendicular-self diffusion coefficient was found to be affected towards the pore from the addition of moisture. It can be seen from Figure 26 that addition of moisture increases the perpendicular self-diffusion coefficient of methane near the wall. This could be due to the fact that

the presence of water molecules along with the already present CO_2 molecules result in even less active sites for CH_4 to adsorb on to, which is not the preferred component for adsorption in the first place. As such, near the wall an increase in the perpendicular self-diffusion coefficient of CH_4 is observed. For CO_2, an increase in perpendicular self-diffusion coefficient is also observed. The water molecules would more preferably adsorb on to the high energy active sites and the CO_2 will adsorb on to the relatively lower energy active sites. This is because water will adsorb on to the silica preferentially and form hydrogen bonds. As such, being adsorbed onto relatively lower energy active sites, the perpendicular self-diffusion coefficient of CO_2 at the wall is found to increase. At the middle of the pore, the perpendicular self-diffusion coefficient is relatively same irrespective of the addition of moisture.

When comparing Figures 27 and 28 to Figures 4 and 5 respectively, one can see a drop in adsorption capacity of *n*-octane and *n*-decane by 29.6% and 25.4% respectively. In both systems, the moisture is found adsorbed completely towards the wall.

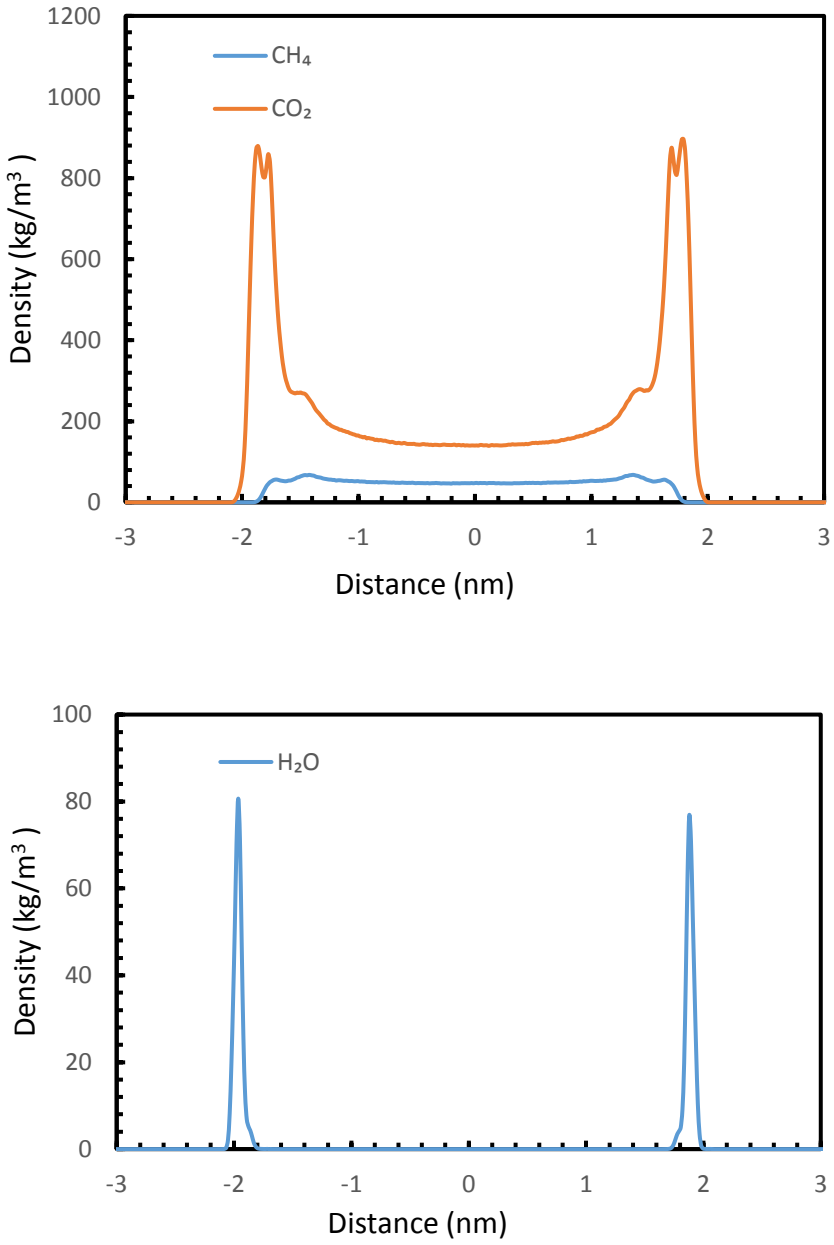

Figure 25: Top) Density Profile of Methane and CO_2 in 4 nm Silica Pore. Bottom) Density Profile of H_2O

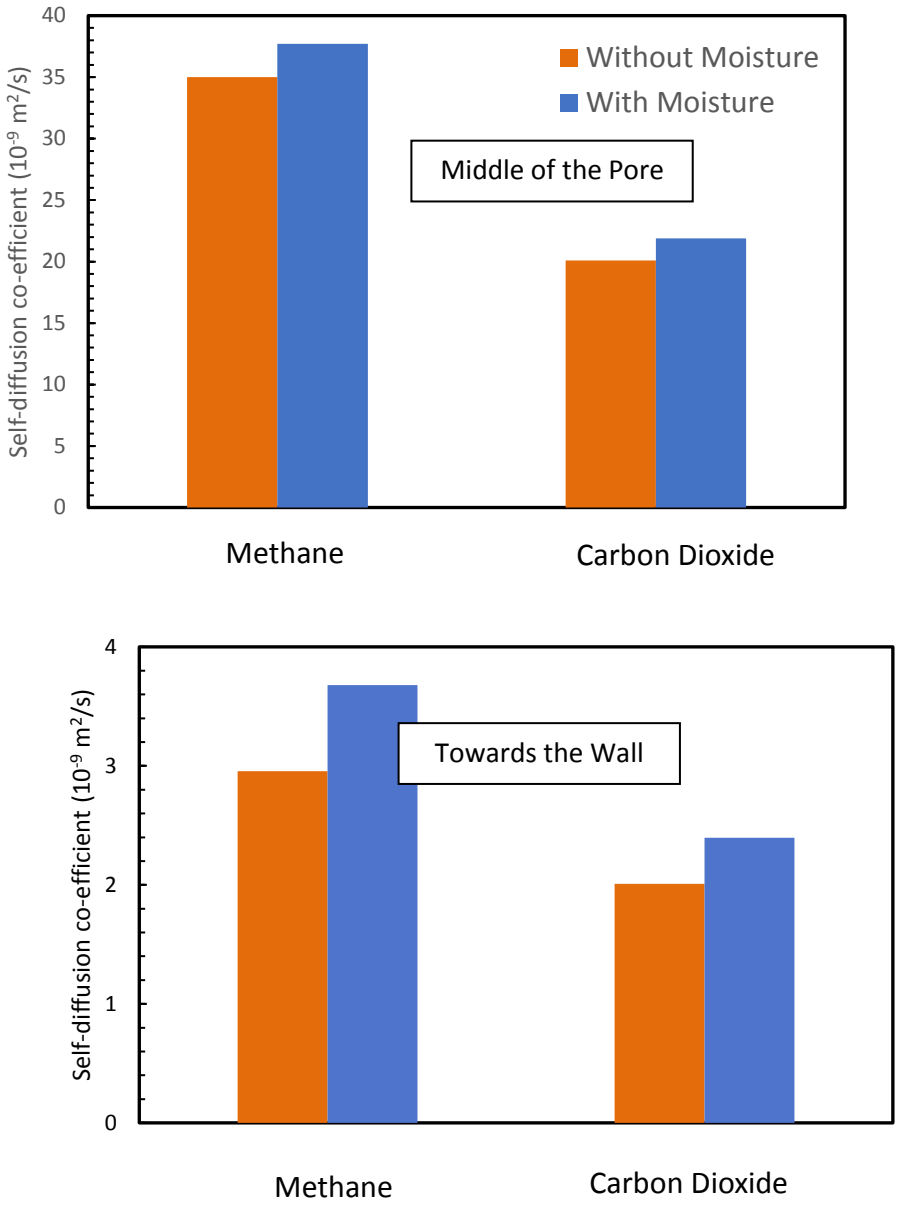

Figure 26: Top) Perpendicular Self-Diffusion Coefficient of Methane and CO2 with Moisture (Blue) and without Moisture (Red): Top) Middle of the pore, Bottom) Towards the wall

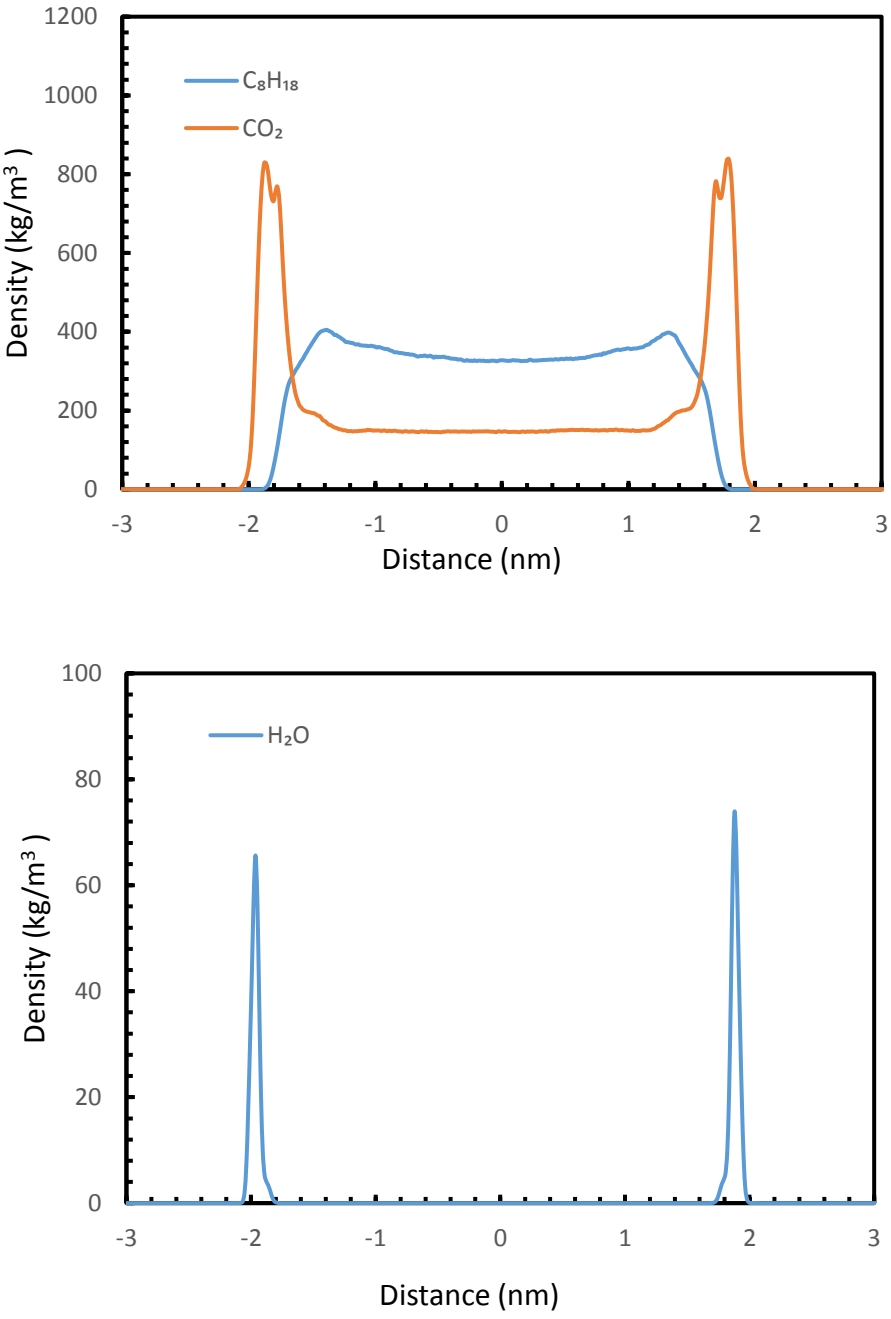

Figure 27: Top) Density Profile of n-octane and CO2 in 4 nm Silica Pore. Bottom) Density Profile of H2O

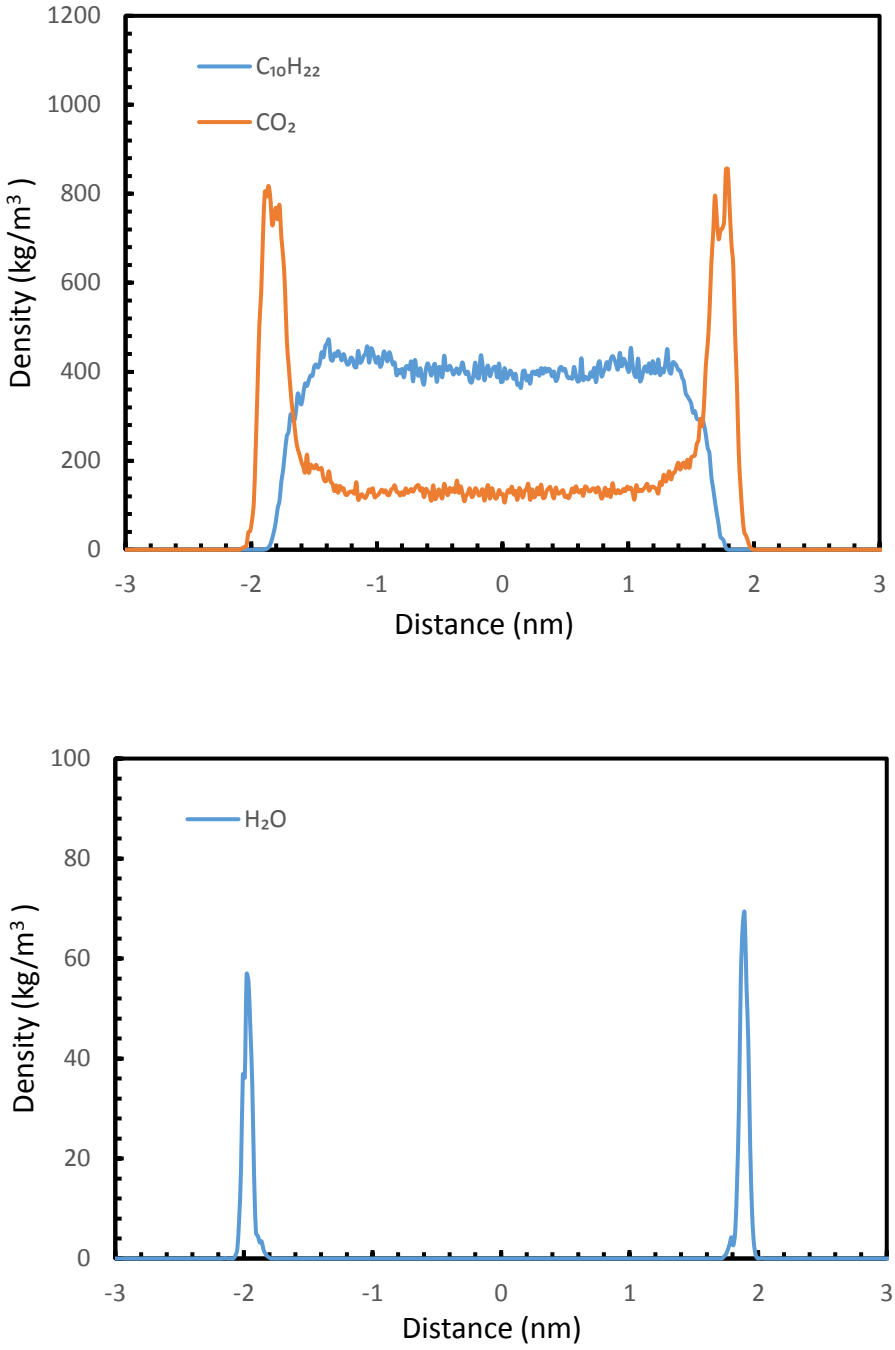

Figure 28: Top) Density Profile of *n*-decane and CO_2 in 4 nm Silica Pore. Bottom) Density Profile of H_2O

4.9 Study of Confinement Using Equation of State

Various systems were studied using SAFT-VR Mie in confinement. Using equations of state can prove quite to be quite useful to study systems under confinement which can be rather time consuming if studied via experimentation and fairly computationally heavy if studied using molecular dynamics simulation. As such, equations of state can prove to be the balance. As such, this chapter builds on the work of Dawas *et al.*[63] and utilizes the capabilities of SAFT-VR Mie in predicting the effect of confinement on single components and mixtures.

The first set of systems analyzed is methane in a 3 nm carbon nanopore and at a temperature of 300 K and three different bulk densities: 0.1 kg/m^3, 1 kg/m^3 and 10 kg/m^3. The results were compared to that obtained from Peng Robinson equation of state as well as those obtained from Monte Carlo (MC) simulations. From figure 29, it can be seen that at the lowest bulk density which is 0.1 kg/m^3, the results between PR EOS, SAFT-VR Mie and MC simulation are agreeable. However, upon increasing the density, although the results from the two EOS remain comparable, there is a noticeable and increasing difference when compared to the results from MC simulations. The reason for this is that the highest local density that can be obtained from equations of state is the packing density which takes into account void spaces between the molecules. Such a limitation does not exist within molecular simulations. The packing density simply represents how the molecules are packed in a specific region and the volume would consider voids or empty spaces as well. As such, equations of state may not provide accurate quantitative results if one is studying systems consisting of densities greater than the packing density but do provide an accurate qualitative description of how the system would behave.

The second system that was analyzed was an equimolar mixture of methane and propane at a pore width of 10 nm at a temperature of 323.15 K and a pressure of 0.5 MPa. Figure 30 shows the mole fraction propane, plotted against the distance from the pore wall. The results compare well with the ones reported by Li *et al.*[65] using DFT model. The third set of systems was to understand the local density profiles of methane at different pressures of 0.1, 1, and 2 MPa at a temperature of 298 K and pore size of 2 nm. The results are in agreement with the ones from Peng Robinson as reported by Dawass *et al.*[63]. The results are shown in figure 31.

In summary, the results obtained by SAFT-VR Mie are able to provide accurate insight from a qualitative perspective as to how a system under confinement would behave. If a system has molecules in a particular region that exceeds the packing density, then the density profile will not be as quantitatively accurate compared to MC simulations owing to the difference in the underlying physics between the two models.

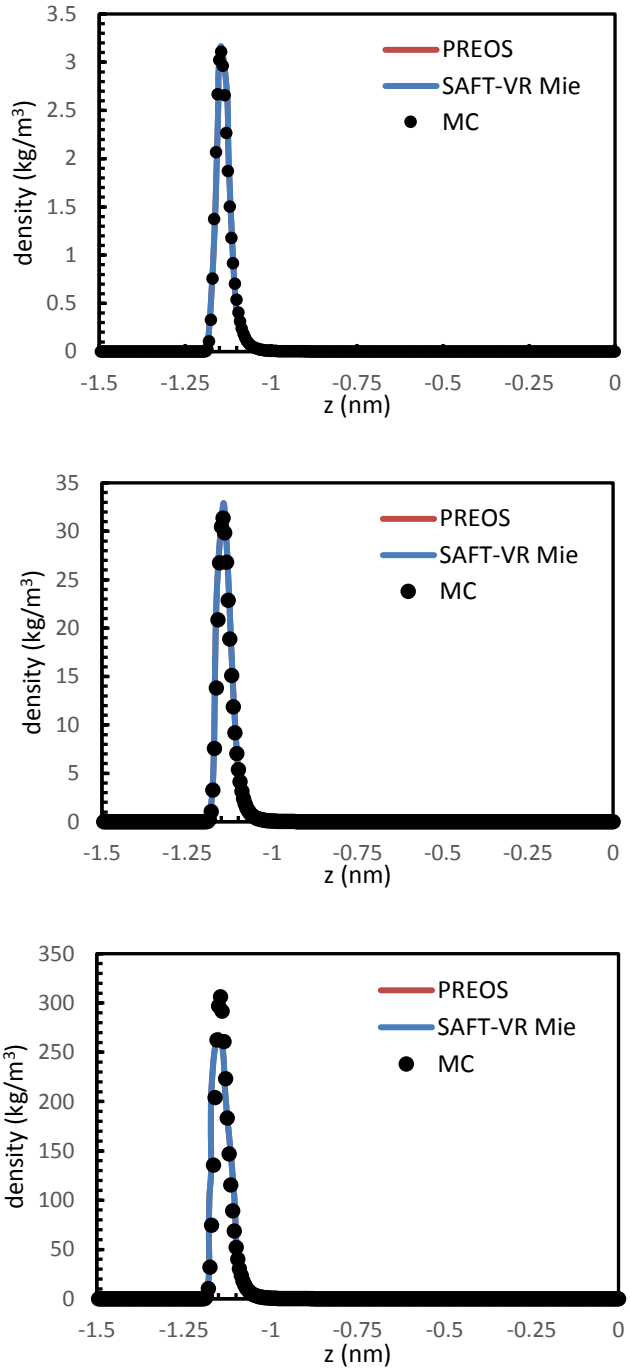

Figure 29: Density Profile in a 3 nm Carbon Pore and Different Bulk Densities: Top) 0.1 kg/m^3, Middle) 1 kg/m^3, Bottom) 10 kg/m^3

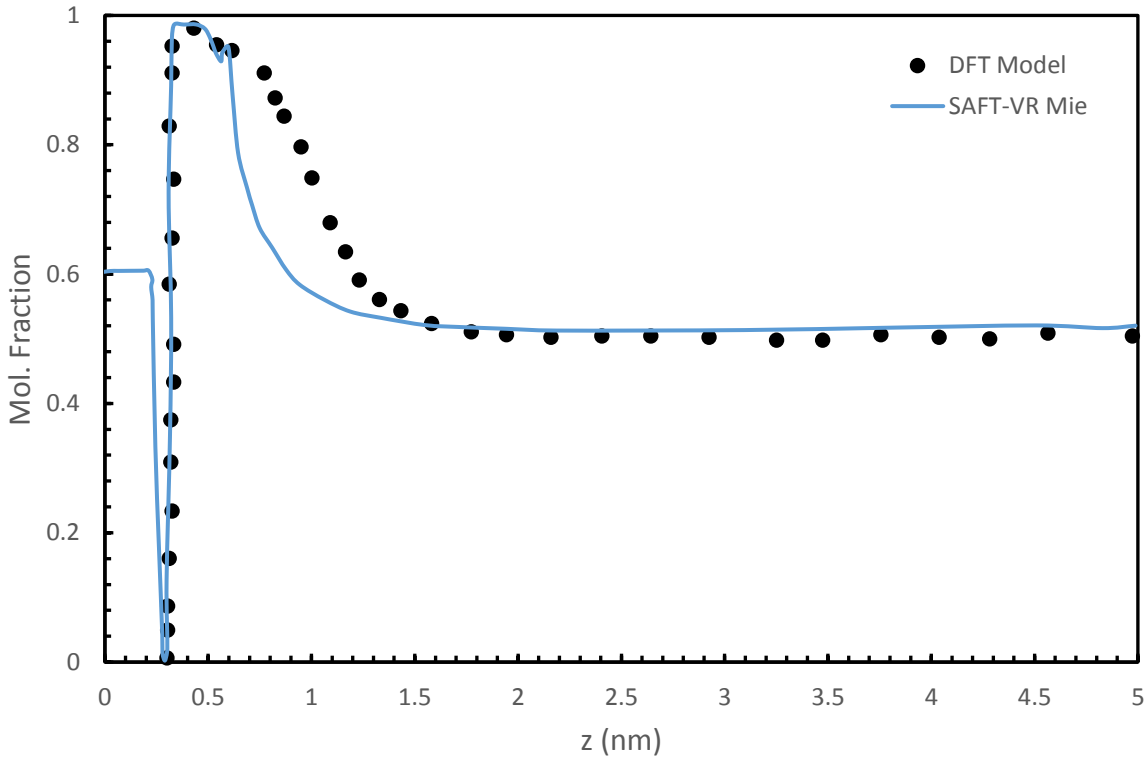

Figure 30: Molar Composition of Propane in a Methane / Propane Mixture, within a 10 nm pore

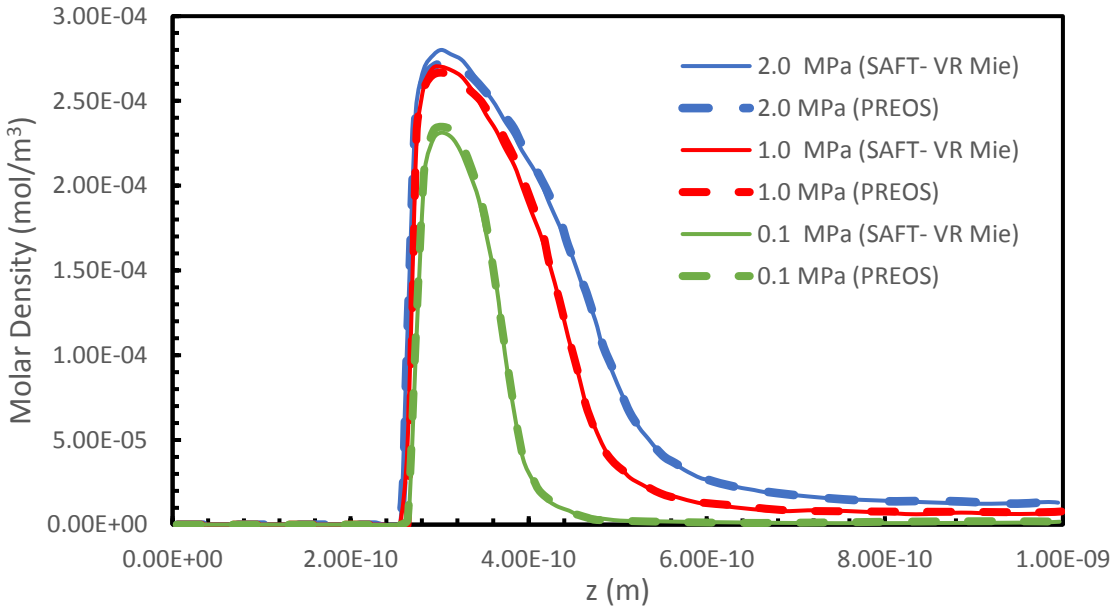

Figure 31: Density Profiles of Methane in a 2 nm Carbon Nanopore, at 298 K and Different Pressures (Graph Provided by Dr. Marcelo Castier, Texas A&M University)

CHAPTER V

CONCLUSIONS AND FUTURE WORK

Molecular dynamic simulation is a useful and proven tool used to understand the effect of confinement on hydrocarbon / CO_2 mixtures. The effect of mixture density, concentration, system temperature, pore size, pore material and moisture was studied. Furthermore, instead of the traditional method of calculating the self-diffusion coefficient using the Einstein relation, a new method was used which allowed for the calculation of self-diffusivity locally, within specific regions of the pore. As such, the effect of various system characteristics was observed at the center of the pore as well as toward the pore wall.

In general, increasing the density of the mixture was found to decrease the perpendicular self-diffusion coefficient. This was observed at the center of the pore as well as in the adsorbed layer. Increasing the temperature of the system increases the mobility of the particles and results in greater self-diffusivity in the perpendicular direction. Changing the concentration has a varying effect in different regions. The self-diffusion coefficient of methane was found to decrease at the center of the pore, as the amount of methane in the system was increased. The same trend was observed towards the pore wall. The perpendicular self-diffusion coefficient of CO_2 decreased at the center of the pore with increasing concentration of CO_2, however, actually increased towards the wall of the pore as more CO_2 adsorbed onto the weak active sites. The pore size also increases the perpendicular self-diffusion coefficient of both components. Including moisture into the system increased the self-diffusivity of the components in the adsorbed layer, however, it had negligible effects towards the center of the pore. This was contradictory to results reported in literature, whereby the general diffusivity was shown to decrease with increasing moisture content.

This work also showed that pore material plays a critical role in shaping the self-diffusivity of the components.

In all cases, the inorganic component preferably adsorbed onto the inorganic pore walls and the organic component, the hydrocarbon, was pushed towards the center of the pore, thus increasing its mobility. As the substrate materials were inorganic in nature, such a behavior was expected as CO_2 would be more strongly attracted to the different substrate materials due to polar interactions. This shows that re-injecting CO_2 into reservoirs can be a feasible method for tertiary oil and / or gas recovery.

Furthermore, SAFT-VR Mie was also used to study the effects of confinement. It was shown that equations of state are useful in providing a qualitative description of how a system will behave. This is useful to a certain degree and is not very computationally heavy when compared to molecular simulations. The equations of state however is limited by the packing density which results in void spaces between molecules being taken into account.

In terms of building on this work, it is important to study the effect of the same parameters on the parallel self-diffusion coefficient as well. This will provide further insight of the transport dynamics of hydrocarbon within such tight pores, especially upon injecting CO_2. This work can potentially then be translated into better predicting elements of reservoir production.

REFERENCES

1. Markewitz, P., Kuckshinrichs, W., Leitner, W., Linssen, J., Zapp, P., Bongartz, R., Schreiber. A., & Müller, T. E. (2012). Worldwide innovations in the development of carbon capture technologies and the utilization of CO2. *Energy & Environmental Science, 5*(6), 7281

2. Li, L., Zhao, N., Wei, W., & Sun, Y. (2013). A review of research progress on CO2 capture, storage, and utilization in Chinese Academy of Sciences. *Fuel, 108*, 112-130

3. Cuéllar-Franca, R. M., & Azapagic, A. (2015). Carbon capture, storage and utilisation technologies: A critical analysis and comparison of their life cycle environmental impacts. *Journal of CO2 Utilization, 9*, 82-102.

4. Luqman, A., & Moosavi, A. (2016). The Impact of CO2 Injection for EOR & its Breakthrough on Corrosion and Integrity of New and Existing Facilities. *Abu Dhabi International Petroleum Exhibition & Conference*.

5. Rogers, J. D., & Grigg, R. B. (2000). A Literature Analysis of the WAG Injectivity Abnormalities in the CO2 Process. *SPE/DOE Improved Oil Recovery Symposium*.

6. Liu, G., Sorensen, J., Braunberger, J., Klenner, R., Ge, J., Gorecki, C., Steadman, E., & Harju, J. (2014). CO2-Based Enhanced Oil Recovery from Unconventional Reservoirs: A Case Study of the Bakken Formation. *SPE Unconventional Resources Conference.*

7. Loucks, R. G., Reed, R. M., Ruppel, S. C., & Jarvie, D. M. (2009). Morphology, Genesis, and Distribution of Nanometer-Scale Pores in Siliceous Mudstones of the Mississippian Barnett Shale. *Journal of Sedimentary Research, 79*(12), 848-861.

8. Zou, C., Yang, Z., Cui, J., Zhu, R., Hou, L., Tao, S., Yuan, X., Wu, S., Lin, S., Wang, L., Bai, B., & Yao, J. (2013). Formation mechanism, geological characteristics and development strategy of nonmarine shale oil in China. *Petroleum Exploration and Development, 40*(1), 15-27.

9. Tang, X., Zhang, J., Wang, X., Yu, B., Ding, W., Xiong, J., Yang, Y., Wang. L., & Yang, C. (2014). Shale characteristics in the southeastern Ordos Basin, China: Implications for hydrocarbon accumulation conditions and the potential of continental shales. *International Journal of Coal Geology, 128-129*, 32-46.

10. Zou, C., Yang, Z., Tao, S., Yuan, X., Zhu, R., Hou, L., Wu, S., Sun, L., Zhang, G., Bai, B., Wang, L., Gao, X., & Pang, Z. (2013). Continuous hydrocarbon accumulation over a large area as a distinguishing characteristic of unconventional petroleum: The Ordos Basin, North-Central China. *Earth-Science Reviews, 126*, 358-369.

11. What is Shale Gas?: Energy Information Administration. (2016). *Alternative Energy and Shale Gas Encyclopedia*, 692-694.

12. Lee, K. S., & Kim, T. H. (2016). Integrative Understanding of Shale Gas Reservoirs. *SpringerBriefs in Applied Sciences and Technology*.

13. Nagarajan, N., & Robinson, R. L. (1987). Equilibrium phase compositions, phase densities, and interfacial tensions for carbon dioxide hydrocarbon systems. 3. CO2 cyclohexane. 4. CO2 benzene. *Journal of Chemical & Engineering Data, 32*(3), 369-371

14. Shaver, R., Robinson, R., & Gasem, K. (2001). An automated apparatus for equilibrium phase compositions, densities, and interfacial tensions: Data for carbon dioxide + decane. *Fluid Phase Equilibria, 179*(1-2), 43-66.

15. Reamer, H., Sage, B., & Lacey, W. (1950). Correction - "Phase Equilibria in Hydrocarbon Systems. Volumetric and Phase Behavior of the Methane-Propane System". *Industrial & Engineering Chemistry, 42*(6), 1258-1258

16. Georgiadis, A., Llovell, F., Bismarck, A., Blas, F. J., Galindo, A., Maitland, G. C., . . . Jackson, G. (2010). Interfacial tension measurements and modelling of (carbon dioxide n-alkane) and (carbon dioxide water) binary mixtures at elevated pressures and temperatures. *The Journal of Supercritical Fluids, 55*(2), 743-754.

17. Wang, L., Neeves, K., Yin, X., & Ozkan, E. (2014). Experimental Study and Modeling of the Effect of Pore Size Distribution on Hydrocarbon Phase Behavior in Nanopores. *SPE Annual Technical Conference and Exhibition*.

18. Prausnitz, J. M., Lichtenthaler, R. N., & De Azevedo, E. C. (2009). *Molecular thermodynamics of fluid-phase equilibria*. Upper Saddle River, N.J: Prentice Hall PTR..

19. Le, T., Striolo, A., & Cole, D. R. (2015). CO2–C4H10 Mixtures Simulated in Silica Slit Pores: Relation between Structure and Dynamics. *The Journal of Physical Chemistry C, 119*(27), 15274-15284.

20. Phan, A., Cole, D. R., & Striolo, A. (2014). Aqueous Methane in Slit-Shaped Silica Nanopores: High Solubility and Traces of Hydrates. *The Journal of Physical Chemistry C, 118*(9), 4860-4868.

21. Ho, T. A., Argyris, D., Papavassiliou, D. V., Striolo, A., Lee, L. L., & Cole, D. R. (2011). Interfacial water on crystalline silica: A comparative molecular dynamics simulation study. *Molecular Simulation, 37*(3), 172-195.

22. Cygan, R. T., Liang, J., & Kalinichev, A. G. (2004). Molecular Models of Hydroxide, Oxyhydroxide, and Clay Phases and the Development of a General Force Field. *The Journal of Physical Chemistry B, 108*(4), 1255-1266.

23. Emami, F. S., Puddu, V., Berry, R. J., Varshney, V., Patwardhan, S. V., Perry, C. C., & Heinz, H. (2015). Correction to Force Field and a Surface Model Database for Silica to Simulate Interfacial Properties in Atomic Resolution. *Chemistry of Materials, 28*(1), 406-407.

24. Cruz-Chu, E. R., Aksimentiev, A., & Schulten, K. (2006). Water−Silica Force Field for Simulating Nanodevices. *The Journal of Physical Chemistry B, 110*(43), 21497-21508.

25. Duin, A. C., Strachan, A., Stewman, S., Zhang, Q., Xu, X., & Goddard, W. A. (2003). ReaxFFSiOReactive Force Field for Silicon and Silicon Oxide Systems. *The Journal of Physical Chemistry A, 107*(19), 3803-3811.

26. Santos, M. S., Franco, L. F., Castier, M., & Economou, I. G. (2018). Molecular Dynamics Simulation of n-Alkanes and CO2 Confined by Calcite Nanopores. *Energy & Fuels, 32*(2), 1934-1941.

27. Bui, T., Phan, A., Cole, D. R., & Striolo, A. (2017). Transport Mechanism of Guest Methane in Water-Filled Nanopores. *The Journal of Physical Chemistry C, 121*(29), 15675-15686.

28. Wang, S., Feng, Q., Zha, M., Javadpour, F., & Hu, Q. (2017). Supercritical Methane Diffusion in Shale Nanopores: Effects of Pressure, Mineral Types, and Moisture Content. *Energy & Fuels,32*(1), 169-180.

29. Wang, R., Peng, F., Song, K., Feng, G., & Guo, Z. (2018). Molecular dynamics study of interfacial properties in CO 2 enhanced oil recovery. *Fluid Phase Equilibria, 467*, 25-32.

30. Jones, J. E. (1924). On the Determination of Molecular Fields. II. From the Equation of State of a Gas. *Proceedings of the Royal Society A: Mathematical, Physical and Engineering Sciences,106*(738), 463-477.

31. Hess, B., Kutzner, C., Spoel, D. V., & Lindahl, E. (2008). GROMACS 4: Algorithms for Highly Efficient, Load-Balanced, and Scalable Molecular Simulation. *Journal of Chemical Theory and Computation, 4*(3), 435-447.

32. Martin, M. G., & Siepmann, J. I. (1998). Transferable Potentials for Phase Equilibria. 1. United-Atom Description of n-Alkanes. *The Journal of Physical Chemistry B, 102*(14), 2569-2577.

33. Potoff, J. J., & Siepmann, J. I. (2001). Vapor–liquid equilibria of mixtures containing alkanes, carbon dioxide, and nitrogen. *AIChE Journal, 47*(7), 1676-1682.

34. Edholm, O., Berendsen, H., & Ploeg, P. V. (1983). Conformational entropy of a bilayer membrane derived from a molecular dynamics simulation. *Molecular Physics, 48*(2), 379-388.

35. Berthelot, D. Sur Le Mélange Des Gaz. (1898). *Comptes rendus Hebdomadaires des Seá nces de l'Acadeḿ ie des Sciences*, 126, 1703−1855.

36. Lorentz, H. A. (1881). Ueber Die Anwendung Des Satzes Vom Virial in Der Kinetischen Theorie Der Gase. *Ann. Phys*. 248(4), 127-136.

37. Xiao, S., Edwards, S. A., & Gräter, F. (2011). A New Transferable Forcefield for Simulating the Mechanics of CaCO3 Crystals. *The Journal of Physical Chemistry C, 115*(41), 20067-20075

38. Argyris, D.; Tummala, N. R.; Striolo, A.; Cole, D. R. (2008). Molecular Structure and Dynamics in Thin Water Films at the Silica and Graphite Surfaces. *J. Phys. Chem.* C, 112(35), 13587−13599.

39. Argyris, D.; Ho, T.; Cole, D. R.; Striolo, A. (2011). Molecular Dynamics Studies of Interfacial Water at the Alumina Surface. *J. Phys. Chem.* C, 115(5), 2038−2046.

40. Phan, A.; Cole, D. R.; Striolo, A. (2014). Preferential Adsorption from Liquid Water-Ethanol Mixtures in Alumina Pores. *Langmuir*, 30(27), 8066−8077.

41. Causa, M.; Dovesi, R.; Pisani, C.; Roetti, C. AB Initio Hartree-` Fock Study of the MgO(001) *Surface. Surf. Sci*. 1986, 175, 551−560.

42. Scamehorn, C. A.; Hess, a. C.; McCarthy, M. I. (1993). Correlation Corrected Periodic Hartree−Fock Study of the Interactions between Water and the (001) Magnesium Oxide Surface. *J. Chem. Phys*., 99(4), 2786.

43. Ho, T. A. (2016). Water and Methane in Shale Rocks: Flow Pattern Effects on Fluid Transport and Pore Structure. *Springer Theses Nanoscale Fluid Transport,* 53-64.

44. Liu, P., Harder, E., & Berne, B. J. (2004). On the Calculation of Diffusion Coefficients in Confined Fluids and Interfaces with an Application to the Liquid−Vapor Interface of Water†. *The Journal of Physical Chemistry B, 108*(21), 6595-6602.

45. Franco, L. F., Castier, M., & Economou, I. G. (2016). Diffusion in Homogeneous and in Inhomogeneous Media: A New Unified Approach. *Journal of Chemical Theory and Computation,12*(11), 5247-5255

46. NIST Webbook. (n.d.). Retrieved May 10, 2018, from https://webbook.nist.gov/.

47. Jorgensen, W. L. (1981). Quantum and statistical mechanical studies of liquids. 11. Transferable intermolecular potential functions. Application to liquid methanol including internal rotation. *Journal of the American Chemical Society, 103*(2), 341-345.

48. Compton, D. A., Montero, S., & Murphy, W. F. (1981). Low-frequency Raman spectrum and asymmetric potential function for internal rotation of gaseous *n*-butane. *The Journal of Physical Chemistry, 84*(26), 3587-3591.

49. Le, T., Ogbe, S., Striolo, A., & Cole, D. R. (2015). N-octane diffusivity enhancement via carbon dioxide in silica slit-shaped nanopores – a molecular dynamics simulation. *Molecular Simulation,42*(9), 745-752.

50. Bródka, A., & Zerda, T. W. (1996). Properties of liquid acetone in silica pores: Molecular dynamics simulation. *The Journal of Chemical Physics, 104*(16), 6319-6326.

51. Franco, L. F., Castier, M., & Economou, I. G. (2016). Anisotropic parallel self-diffusion coefficients near the calcite surface: A molecular dynamics study. *The Journal of Chemical Physics*, *145*(8), 084702.

52. Khosrokhavar, R., Wolf, K.-H., Bruining, H. (2014). "Sorption of CH4 and CO2 on Belgium Carboniferous Shale Using a Manometric Set-Up." *International Journal of Coal Geology*, pp. 153-161.

53. Gasparik, M., Ghanizadeh, A., Gensterblum, Y., & Krooss, B. M. (2013). "Multi-temperature" method for high-pressure sorption measurements on moist shales. *Review of Scientific Instruments,84*(8), 085116.

54. Cavenati, S., Grande, C. A., & Rodrigues, A. E. (2004). Adsorption Equilibrium of Methane, Carbon Dioxide, and Nitrogen on Zeolite 13X at High Pressures. *Journal of Chemical & Engineering Data, 49*(4), 1095-1101.

55. Zhu, J., Jessen, K., Kovscek, A. R., & Orr, F. M. (2003). Analytical Theory of Coalbed Methane Recovery by Gas Injection. *SPE Journal, 8*(04), 371-379.

56. Duan, S., Gu, M., Du, X., & Xian, X. (2016). Adsorption Equilibrium of CO2 and CH4 and Their Mixture on Sichuan Basin Shale. *Energy & Fuels, 30*(3), 2248-2256.

57. Denney, D. (2011). Carbon Dioxide Storage Capacity of Organic-Rich Shales. *Journal of Petroleum Technology, 63*(07), 114-117.

58. Gensterblum, Y., Busch, A., & Krooss, B. M. (2014). Molecular concept and experimental evidence of competitive adsorption of H2O, CO2 and CH4 on organic material. *Fuel, 115*, 581-588.

59. Mamora, D., & Seo, J. (2002). Enhanced Gas Recovery by Carbon Dioxide Sequestration in Depleted Gas Reservoirs. *Proceedings of SPE Annual Technical Conference and Exhibition*.

60. Eliebid, M., Mahmoud, M., Shawabkeh, R., Elkatatny, S., & Hussein, A. I. (2018). Effect of CO_2 Adsorption on Enhanced Natural Gas Recovery and Sequestration in Carbonate Reservoirs. *Journal of Natural Gas Science and Engineering, 55*, 575-584

61. Travalloni, L., Castier, M., Tavares, F. W., & Sandler, S. I. (2010). Thermodynamic modeling of confined fluids using an extension of the generalized van der Waals theory. *Chemical Engineering Science, 65*(10), 3088-3099.

62. Tan, S. P., & Piri, M. (2015). Equation-of-state modeling of associating-fluids phase equilibria in nanopores. *Fluid Phase Equilibria, 405*, 157-166.

63. Dawass, N., D'Lima, M. L., Economou, I. G., & Castier, M. (2016). Phase Equilibrium with External Fields: Application to Confined Fluids. *Journal of Chemical & Engineering Data, 61*(8), 2873-2885.

64. Pan, Z., Connell, L. D., Camilleri, M., & Connelly, L. (2010). Effects of matrix moisture on gas diffusion and flow in coal. *Fuel, 89*(11), 3207-3217.

65. Li, Z., Jin, Z., & Firoozabadi, A. (2014). Phase Behavior and Adsorption of Pure Substances and Mixtures and Characterization in Nanopore Structures by Density Functional Theory. *SPE Journal,19*(06), 1096-1109.

APPENDIX A

LIST OF SIMULATIONS

Serial No.	Simulation Description
1	50 kg/m^3 equimolar mixture of CH_4 – CO_2 at 375 K in 3 nm silica pore
2	100 kg/m^3 equimolar mixture of CH_4 – CO_2 at 375 K in 3 nm silica pore
3	150 kg/m^3 equimolar mixture of CH_4 – CO_2 at 375 K in 3 nm silica pore
4	200 kg/m^3 equimolar mixture of CH_4 – CO_2 at 375 K in 3 nm silica pore
5	250 kg/m^3 equimolar mixture of CH_4 – CO_2 at 375 K in 3 nm silica pore
6	300 kg/m^3 equimolar mixture of CH_4 – CO_2 at 375 K in 3 nm silica pore
7	50 kg/m^3 equimolar mixture of CH_4 – CO_2 at 375 K in 4 nm silica pore
8	100 kg/m^3 equimolar mixture of CH_4 – CO_2 at 375 K in 4 nm silica pore
9	150 kg/m^3 equimolar mixture of CH_4 – CO_2 at 375 K in 4 nm silica pore
10	200 kg/m^3 equimolar mixture of CH_4 – CO_2 at 375 K in 4 nm silica pore
11	250 kg/m^3 equimolar mixture of CH_4 – CO_2 at 375 K in 4 nm silica pore
12	300 kg/m^3 equimolar mixture of CH_4 – CO_2 at 375 K in 4 nm silica pore
13	50 kg/m^3 equimolar mixture of CH_4 – CO_2 at 375 K in 8 nm silica pore
14	100 kg/m^3 equimolar mixture of CH_4 – CO_2 at 375 K in 8 nm silica pore
15	150 kg/m^3 equimolar mixture of CH_4 – CO_2 at 375 K in 8 nm silica pore
16	200 kg/m^3 equimolar mixture of CH_4 – CO_2 at 375 K in 8 nm silica pore
17	250 kg/m^3 equimolar mixture of CH_4 – CO_2 at 375 K in 8 nm silica pore
18	300 kg/m^3 equimolar mixture of CH_4 – CO_2 at 375 K in 8 nm silica pore
19	50 kg/m^3 2:1 (molar) mixture of CH_4 – CO_2 at 375 K in 4 nm silica pore
20	100 kg/m^3 2:1 (molar) mixture of CH_4 – CO_2 at 375 K in 4 nm silica pore
21	150 kg/m^3 2:1 (molar) mixture of CH_4 – CO_2 at 375 K in 4 nm silica pore
22	200 kg/m^3 2:1 (molar) mixture of CH_4 – CO_2 at 375 K in 4 nm silica pore
23	250 kg/m^3 2:1 (molar) mixture of CH_4 – CO_2 at 375 K in 4 nm silica pore
24	300 kg/m^3 2:1 (molar) mixture of CH_4 – CO_2 at 375 K in 4 nm silica pore
25	50 kg/m^3 1:2 (molar) mixture of CH_4 – CO_2 at 375 K in 4 nm silica pore
26	100 kg/m^3 1:2 (molar) mixture of CH_4 – CO_2 at 375 K in 4 nm silica pore
27	150 kg/m^3 1:2 (molar) mixture of CH_4 – CO_2 at 375 K in 4 nm silica pore
28	200 kg/m^3 1:2 (molar) mixture of CH_4 – CO_2 at 375 K in 4 nm silica pore
29	250 kg/m^3 1:2 (molar) mixture of CH_4 – CO_2 at 375 K in 4 nm silica pore
30	300 kg/m^3 1:2 (molar) mixture of CH_4 – CO_2 at 375 K in 4 nm silica pore
31	450 kg/m^3 1:2 (molar) mixture of CO_2 – nC_8H_{20} at 375 K in 4 nm silica pore
32	550 kg/m^3 1:2 (molar) mixture of CO_2 – nC_8H_{20} at 375 K in 4 nm silica pore
33	650 kg/m^3 1:2 (molar) mixture of CO_2 – nC_8H_{20} at 375 K in 4 nm silica pore
34	450 kg/m^3 1:2 (molar) mixture of CO_2 – $nC_{10}H_{22}$ at 375 K in 4 nm silica pore
35	550 kg/m^3 1:2 (molar) mixture of CO_2 – $nC_{10}H_{22}$ at 375 K in 4 nm silica pore
36	650 kg/m^3 1:2 (molar) mixture of CO_2 – $nC_{10}H_{22}$ at 375 K in 4 nm silica pore
Serial No.	**Simulation Description**

37	300 kg/m^3 equimolar mixture of CH_4 – CO_2 with 3 mol. % H_2O at 375 K in 4 nm silica pore
38	550 kg/m^3 1:2 (molar) mixture of CO_2 – nC_8H_{20} with 3 mol. % H_2O at 375 K in 4 nm silica pore
39	550 kg/m^3 1:2 (molar) mixture of CO_2 – $nC_{10}H_{22}$ with 3 mol. % H_2O at 375 K in 4 nm silica pore
40	300 kg/m^3 equimolar mixture of CH_4 – CO_2 at 300 K in 4 nm silica pore
41	300 kg/m^3 equimolar mixture of CH_4 – CO_2 at 450 K in 4 nm silica pore
42	350 kg/m^3 CH_4 at 300 K in 10 nm silica pore
43	350 kg/m^3 CH_4 at 300 K in 10 nm muscovite pore
44	350 kg/m^3 CH_4 at 300 K in 10 nm magnesium oxide pore
45	350 kg/m^3 CH_4 at 300 K in 10 nm alumina pore
46	350 kg/m^3 CH_4 at 300 K in 10 nm calcite pore
47	350 kg/m^3 C_2H_6 at 300 K in 10 nm silica pore
48	350 kg/m^3 C_2H_6 at 300 K in 10 nm muscovite pore
49	350 kg/m^3 C_2H_6 at 300 K in 10 nm magnesium oxide pore
50	350 kg/m^3 C_2H_6 at 300 K in 10 nm alumina pore
51	350 kg/m^3 C_2H_6 at 300 K in 10 nm calcite pore
52	350 kg/m^3 4:1 (molar) mixture of CH_4 – C_2H_6 at 300 K in 10 nm silica pore
53	350 kg/m^3 4:1 (molar) mixture of CH_4 – C_2H_6 at 300 K in 10 nm muscovite pore
54	350 kg/m^3 4:1 (molar) mixture of CH_4 – C_2H_6 at 300 K in 10 nm magnesium oxide pore
55	0.1 kg/m^3 CH_4 at 300 K in 3 nm carbon pore (SAFT-VR Mie)
56	1 kg/m^3 CH_4 at 300 K in 3 nm carbon pore (SAFT-VR Mie)
57	10 kg/m^3 CH_4 at 300 K in 3 nm carbon pore (SAFT-VR Mie)
58	Equimolar mixture of CH_4 – C_3H_8 at 323.15 K and 0.5 MPa in 10 nm carbon pore (SAFT-VR Mie)
59	CH_4 at 298 K and 0.1 MPa in 2 nm carbon pore (SAFT-VR Mie)
60	CH_4 at 298 K and 1 MPa in 2 nm carbon pore (SAFT-VR Mie)
61	CH_4 at 298 K and 2 MPa in 2 nm carbon pore (SAFT-VR Mie)